Electronic and Thin Film Stacking Structure of Organic Semiconductors

A Thesis Submitted to the College of

Graduate Studies and Research

In Partial Fulfillment of the Requirements

For the Degree Master of Science

In the Department of Physics and Engineering Physics

University of Saskatchewan

Saskatoon

By

Paul Bazylewski

Permission to Use

In presenting this thesis in partial fulfilment of the requirements for a Postgraduate degree from the University of Saskatchewan, I agree that the Libraries of this University may make it freely available for inspection. I further agree that permission for copying of this thesis in any manner, in whole or in part, for scholarly purposes may be granted by Dr. Gap Soo Chang or, in their absence, by the Head of the Department or the Dean of the College in which my thesis work was done. It is understood that any copying or publication or use of this thesis or parts thereof for financial gain shall not be allowed without my written permission. It is also understood that due recognition shall be given to me and to the University of Saskatchewan in any scholarly use which may be made of any material in my thesis.

Requests for permission to copy or to make other use of material in this thesis in whole or part should be addressed to:

Head of the Department of Physics and Engineering Physics
University of Saskatchewan
Saskatoon, Saskatchewan
S7N 5E2

Abstract

Presented here is a study of the electronic properties and molecular stacking structure of four novel X-shaped anthracene based organic semiconductors utilizing near-edge X-ray absorption fine structure (NEXAFS) spectroscopy and density functional theory (DFT) calculations. These materials have been found to exhibit high charge carrier mobility when used in organic thin film transistors without an annealing step. Angle resolved NEXAFS show local molecular order through polarization dependence in C 1*s* → π* transitions, and that the plane of the anthracene core is oriented nearly normal to the plane of the substrate. DFT calculations were used examine electronic structure and the effects of molecular geometry, showing that the highest occupied molecular orbital (HOMO) conjugation extends to the thiophene end groups. The type of attachment of the thiophene end group is determined to modify intermolecular interaction, resulting in either a cofacial or herringbone structure. With the understanding of how these materials form an ordered crystal structure, future fabrication of new materials may be directed towards a preference for crystallization without annealing.

A study with applications for organic photovoltaic devices was also undertaken to examine the thin film stacking structure of [6,6]-phenyl-C_{61}-butyric acid methyl ester (PCBM). NEXAFS measurements show that the side chain lifts the energy degeneracy of the C_{60} molecular orbitals around the chain attachment. This breaks the spatial π -orbital symmetry of the lowest unoccupied molecular orbital (LUMO) of the C_{60} backbone which is observed through polarization dependence of π* transitions. The intensity dependence is further analyzed to determine the bulk crystal structure of PCBM.

Acknowledgements

I would first like to thank my supervisor, Dr. Gap Soo Chang, for all of his guidance, help, and support throughout my degree. His experience and patience with me has made this a truly enjoyable experience. After every conversation with him I always return to work fresh ideas and a renewed sense of excitement about the discoveries just waiting to be made. I would also like to thank my coworkers who share my office. They were always available to bounce ideas off of when I've been thinking in circles and need a jump start.

Last, I would like to thank my amazing family, Jordan and Sophie, for putting up with the long hours of work and many hours of beam time that were required to complete this degree. After a long day at the office, coming home to them makes it possible to get up and do it all again the next day.

CONTENTS

Abstract ii

Acknowledgements iii

List of Tables vi

List of Figures vii

List of Abbreviations ix

1. Introduction 1

2. Background 3

3. Theory 6

- 3.1. Molecular Orbital Theory 6
- 3.2. Density Functional theory 10
  - 3.2.1 The Hohenberg-Kohn Theorems and Kohn–Sham Equations 10
  - 3.2.2. Basis Sets and Exchange-Correlation Functionals 13
- 3.3. Electronic Structure Calculations 13
  - 3.3.1. Simulating NEXAFS spectra with StoBe 14
  - 3.3.2. Energy Calibration 16
  - 3.3.3 Calculating Electronic Structure with GAUSSIAN03 17
- 3.4. Synchrotrons and X-ray Radiation 18
  - 3.4.1. Synchrotron Light and Beamlines 19
  - 3.4.2. X-ray Spectroscopy Techniques 23
  - 3.4.3. XAS and XES 26

4. Experimental 29

- 4.1. Sample Preparation 30
- 4.2. TEY and TFY 32
- 4.3. Angle Resolved NEXAFS 33
- 4.4. Energy Calibration and Normalization 37
- 4.5. Radiation Damage 42

5. Results and Discussion 44

- 5.1. Anthracene-based Organic Semiconductors 44
  - 5.1.1. Thin Film Structure and Charge Carrier Mobility 48
  - 5.1.2. Angle Resolved C 1*s* NEXAFS 50

5.1.3. DFT calculations 54
5.1.4. HOMO-LUMO gap and Organic Semiconductors 58
5.1.5. C *K*α XES and the HOMO 61
5.1.6. Molecular orientation 65
5.1.7. Conclusions 66

5.2. PCBM 67
5.2.2. NEXAFS Measurements 68
5.2.3. DFT calculations 71
5.2.4. Thin Film Stacking Structure 74
5.2.5. HOMO-LUMO Gap 76
5.2.6. Conclusions 78

6. Summary and Future Research 79

6.1. Properties of Materials Studied 79

6.2. Future small molecule systems 80

6.3. Physical Vapor Deposition and Solar Simulation 81

7. References 83

APPENDIX: StoBe Input Files 89

List of Tables

Table 3.1. Selection rules for electric dipole allowed transitions................................ 25

Table 5.1: Measured Hole mobilities calculated from I-V characteristic.................. 52

Table 5.2: HOMO-LUMO gaps determined from XAS/XES compared to UV-Vis. 61

Table 5.3. Tabulated peak intensities for PCBM Angle Resolved NEXAFS............. 70

List of Figures

Figure 3.1. Shapes of *s* and *p* type orbital wave functions and the form of the ethylene molecule 7

Figure 3.2 Example of π-bonding where constructive and destructive interference create bonding and antibonding orbitals. 8

Figure 3.3 Example of σ-bonding through sp^2-type orbitals....................................... 9

Figure 3.4. General schematic of a synchrotron facility, showing (a) Linear Accelerator Stage, (b) Booster Ring, and (c) Storage Ring with beam line hutches attached. [25] 20

Figure 3.5. Schematic representation of the electron beam path and resulting radiation from an insertion device [27]. 21

Figure 3.6. Schematic of Beam line 8.0.1, located at the Advanced Light Source, Berkeley, CA [28]. 22

Figure 3.7. Graphical representation of the XAS and XES processes 26

Figure 4.1. Image of spin coater equipment with nitrogen source attached. 30

Figure 4.2. Schematic representation of the directionality of π* and σ* states for a benzene ring.. 34

Figure 4.3. Angle-resolved NEXAFS measurements of HOPG for normal and near grazing incidence.. 36

Figure 4.4. (a) The raw TEY signal of PDIF-CN2 with the simultaneously measured I_o signal in the insert. (b) The I_o normalized TEY signal. Note the severe distortions to the spectrum with the resonances barely recognizable. (c) The same spectrum normalized with the photodiode beam current, with the photodiode beam current shown in the inset. 41

Figure 5.1. Schematic representations of the four anthracene-based materials, (a) B-ant-HT, (b) B-ant-THT, (c) HB-ant-HT, and (d) HB-ant-THT. Note the structural similarities between them. 45

Figure 5.2. XRD measurements of B-ant-HT and HB-ant-HT thin films fabricated at room temperature without additional annealing. HB-ant-HT shows only one sharp (100) peak, indicating a high degree of structural order. Measurements taken by collaborators at the 8C1 and 3C2 beamlines, Pohang Accelerator Laboratory, South Korea. 46

Figure 5.3. Common stacking structures exhibited by functionalized acenes [46]... 47

Figure 5.4. Angle resolved NEXAFS of the four anthracene-based molecules. Clear evidence of local structure is observed through polarization dependence for those molecules with additional alkyl chains. 53

Figure 5.5. Comparison of HB-ant-HT NEXAFS to Anthracene powder and DFT XAS simulation (top panel). The bottom panel shows the contribution to calculated spectrum from each molecular constituent. 55

Figure 5.6. Comparison of B-ant-THT NEXAFS to DFT simulation (top panel). The bottom panel shows the contribution to calculated spectrum from each molecular constituent. Note the differences in anthracene and thiophene resonances. 57

Figure 5.7. HB-ant-THT XAS and XES measurements. Second derivatives are used to find the C 1*s* →LUMO and HOMO → C 1*s* transitions, with a resulting gap of 2.01 eV. 60

Figure 5.8. XES measurements of the anthracene based materials. Few spectral features are evident, with all measurements appearing very similar. 62

Figure 5.9. HOMO isosurfaces. This MO is extremely similar between all four molecules, and is located primarily on the anthracene, thiophene, and ethynyl groups. 64

.. 64

Figure 5.10. Angle-resolved C 1*s* XAS measurements of PCBM thin film measured in TFY mode. α represents the angle of incidence of X-ray radiation measured from the substrate normal. 69

Figure 5.11. (a) Comparison of C 1*s* XAS spectra of PCBM spin-coated film measured in TFY mode with simulated PCBM spectrum and the measured reference spectrum of C_{60} powder and (b) the calculated XAS spectra for individual groups within PCBM molecule and the inset shows the molecular groups coloured to match the corresponding line colour of simulated spectra. 72

Figure 5.12. Four possible stacking structures that are supported by the angular dependence seen in the NEXAFS measurements. (d) shows an arrangement which allows for stronger hydrogen bonding between functional chains 75

Figure 5.13. PCBM XES and XAS powder spectra, with smoothing applied to the XES. Second derivatives of the smoothed XES and measured XAS spectra are used to determine the energies of the HOMO and LUMO, and a resulting gap of 1.87 eV. 77

List of Abbreviations

NEXAFS	Near-edge X-ray Absorption Fine Structure
DFT	Density Functional Theory
BPEA	9,10-Bis(phenylethynyl)anthracene
OTFT	Organic Thin Film Transistor
HOMO	Highest occupied molecular orbital
LUMO	Lowest unoccupied molecular orbital
OPV	Organic Photovoltaic cell
PCBM	[6,6]-phenyl-C_{61}-butyric acid methyl ester
XES	X-ray Emission Spectroscopy
XAS	X-ray Absorption Spectroscopy
(P(NDI2OD-T2)	poly{[*N*,*N*9-bis(2-octyldodecyl)-naphthalene-1,4,5,8-bis(dicarboximide)-2,6-diyl]-*alt*-5,59-(2,29-bithiophene)}
TFT	Thin Film Transistor
OLED	Organic Light Emitting Diode
OLET	Organic Light Emitting Transistor
MO	Molecular Orbital
LCAO	Linear Combination of Atomic Orbitals
SCF	Self-Consistent Field Method
TZVP	Triple-zeta plus Valence Polarization (basis set)
FWHM	Full-width at Half Maximum
CLS	Canadian Light Source
ALS	Advanced Light Source
SGM	Spherical Grating Monochromator (beam line)
SXF	Soft-X-ray Fluorescence (beam line)
RF	Radio Frequency
DOS	Density of States
NXES	Non-Resonant X-ray Emission Spectroscopy
RIXS	Resonant Inelastic X-ray Scattering
TEY	Total Electron Yield
TFY	Total Fluorescence Yield
P3HT	poly(3-hexylthiophene)
BPDA-PDA	poly(biphenyl dianhydride-*p*-phenlenediamine)
IP	Ionization Potential
HOPG	Highly ordered pyrolytic graphite
PDIF-CN2	N,N-1H,1Herfluorobutyl dicyanoperylenediimide
OTS	Octadecyltrichlorosilane
SAM	Self-Assembled Monolayer
XRD	X-ray Diffraction
CV	Cyclic Voltammetry
AFM	Atomic Force Microscopy
VRH	Variable-Range Hopping
MTR	Multiple Trapping and Release
11-AUT	11-amino-1-undecane thiol
PVD	Physical Vapor Deposition
PFP	Perfluoropentacene

TIPS	6,13-bis(Triisopropylsilylethynyl)-(Pentacene)
STM	Scanning Tunneling Microscopy
MDMO-PPV	Poly(2-methoxy-5-(3’-7’-dimethyloctyloxy)-1,4-phenylenevinylene)

1. Introduction

The primary focus of this manuscript is the study of organic molecular systems using X-ray spectroscopy techniques to investigate both the electronic structure and thin film stacking structure. Two systems are discussed in this study, the first is a set of four novel, recently fabricated 9,10-Bis(phenylethynyl)anthracene (BPEA)-based *p*-type semiconductors for use in organic thin film transistor (OTFT) devices, which uncommonly crystallize with a highly ordered structure in solution-processed thin films without the need for additional annealing. This is a remarkable property rarely found in organic materials, which generally form polycrystalline or completely amorphous films without the use of annealing or other exotic processing techniques. Such materials are of high interest to the organic materials community, as low cost solution processing that can yield high efficiency devices could revolutionize the semiconductor industry and open the door for a host of new devices produced at a fraction of the cost compared to their predecessors. These materials are very similar structurally, but display non-trivial variation in electrical and structural characteristics between them. This study seeks to elucidate the origin of self-organization in these materials, as well as characterize the electronic structure of these molecules in the context of the minor structural differences they present. To this end, X-ray spectroscopic techniques and density functional theory (DFT) calculations are used to examine the properties of these materials, and the thin film structure of each is proposed as well as the origins of self-organization.

The second is the material [6,6]-phenyl-C_{61}-butyric acid methyl ester PCBM, an *n*-type semiconductor material heavily used in organic photovoltaic (OPV) devices. Construction of solar cell devices from organic materials is highly desirable as the comparative cost of solution processing large area semiconductor films is a fraction of that required for the presently available high efficiency silicon-based cells. One of the primary limitations in organic solar cells is the variability of molecular structure in the active layer which harvests solar energy through exciton production. The diffusion of free charge carriers through the semiconductor layer, and consequently the energy conversion efficiency of the device, is highly affected by molecular stacking structure and electronic structure of the materials in the active layer. The effect of the functional chain attachment on bulk stacking and electronic structure for PCBM is examined using a combination of spectroscopic techniques and DFT calculations. The results are used to determine the possible crystal structures of PCBM in thin films, as well as the effect of the functional chain on the distribution of molecular orbitals across the molecule. With knowledge of the distribution of molecular states as well as the preferred self-organizing stacking structure, the behavior of PCBM when blended with other materials may be better predicted. Additionally, these results may be generalized as a starting point for the study of the thin film structure of other functionalized fullerenes (C_{60}).

Following this introduction, a general background is given describing the differences between organic semiconductors and conventional inorganic semiconductors such as silicon. An overview of basic molecular orbital theory and the DFT calculation methods used in this work is then described, followed by a discussion of synchrotron light sources and how they are used to generate light for spectroscopy experiments. A brief outline of the software used to calculate electronic structure is also provided, with a description of the individual calculations that are required to simulate the electronic structure of materials. Next the sample preparation method used to produce thin films is described, as well as the X-ray spectroscopy techniques that were used to study the properties of the thin films. The specific usage of each technique is discussed as well as some practical considerations for experimental measurements such as radiation damage.

2. Background

In the past decade, organic materials have become increasingly popular for use in fabrication of semiconductor devices. Recent progress in the development of organic semiconductor materials for electronic devices has been successful for *p*-type organic semiconductors such as pentacene, rubrene, and thiophene containing polymers which have been used to produce OTFTs showing typical hole mobilities of 1 cm^2/Vs [1]. More recently, similar results have been achieved for *n*-type materials with electron mobility in poly{[*N*,*N*'-bis(2-octyldodecyl)-naphthalene-1,4,5,8-bis(dicarboximide)-2,6-diyl]-*alt*-5,5'-(2,2'-bithiophene)} (P(NDI2OD-T2) up to 0.85 cm^2/Vs [2]. In the context of the possible achievable charge carrier mobility, this is much lower than that of crystalline silicon which has realized a thin film transistor (TFT) mobility two orders of magnitude larger, at 130 cm^2/Vs [3]. The performance of organic electronics is however comparable to amorphous silicon which can obtain mobility of 1.05 cm^2/Vs in highly optimized TFT devices [4]. For this reason, organic materials are not expected to compete with the high mobility and switching speeds of crystalline silicon based devices used for example in computer processors, but rather in applications that take advantage of the unique plastic-like properties of organic materials and do not require high mobility. This includes solar cells, organic light emitting diodes (OLED) or novel light emitting transistors (OLET) [5], which can all be mounted on flexible, transparent substrates. In such applications, organic electronics have the advantage of the processing methods that do not require extreme temperature or atmosphere conditions. In order to produce a high performance silicon based device, the semiconductor layer must be either grown or deposited using a vapor deposition process which requires extensive vacuum equipment and high processing temperatures. By contrast, most organic semiconductors are soluble in common organic solvents - allowing for low cost solution processing which is easily extendable to large area deposition - and also have generally low vaporization temperatures in the range of 200 ~ 400 °C at ambient pressure or lower for high vacuum pressure (10^{-6} torr). Solution processing does not require extreme temperatures or vacuum chambers and has been used with great success to produce functioning devices [6]. A lower processing temperature also immediately allows for a wide variety of transparent or flexible substrates to be used which would not be possible for silicon, which requires high temperature processing.

These are then the advantages of using organic materials in novel applications that would not be possible otherwise, but achievement of these goals comes with a large set of challenges. Organic semiconductors by nature are small molecule or polymer materials that do typically exist in polycrystalline or completely disordered form. In a solid or thin film, the molecules are bonded and organized through Van der Waals forces and molecular dipoles, in a structure that is greatly dependent on the fabrication process used. This is in contrast to non-molecular materials that often form ordered, highly reproducible, strongly covalently bonded crystal structures.

The differences in crystal structure between conventional inorganic and organic materials also give rise to very different electronic structures, and consequently different charge transport properties. Due to this, the theory of band transport which describes the movement of free charge carriers in covalently bonded solids is not applicable to disordered or polycrystalline organics. This has triggered the development of entirely different transport models where charge carriers move by hopping between localized states, but the complete picture of carrier transport remains elusive [7]. Therefore, it is a difficult challenge to explain and optimize the performance of organic materials when the accepted theories of crystallization and charge transport have not been fully investigated, leaving many unknowns in the course of any study.

To date, the main body of research into organic materials has been to examine the properties of individual materials and tailor device fabrication recipes to achieve the highest performance possible. In general, the study centers on three main areas to attempt to achieve high performance devices in the context of high mobility in OTFTs, or high power conversion efficiency in OPVs. These areas are the discovery and synthesis of new organic materials, optimization of structural and morphological characteristics of existing materials, and design of device architectures including peripheral components, such as electrode and dielectric materials in the case of OTFTs [8]. However, with the potentially infinite number of materials that could be synthesized, it is clear that the study of organic electronics that has been achieved thus far is indeed just the tip of the iceberg. Much more work remains to be done to develop complete theories of transport in disordered materials, as well as a clearer understanding of how the various thin film fabrication methods affect device performance.

3. Theory

In the current study, the electronic and structural properties of materials are probed using spectroscopic techniques which measure the effects of electron excitation due to external energy input. In this case, bound electrons are excited by absorption of synchrotron-generated X-rays in the soft energy region. It is generally the subsequent reaction of the system to the excitation as it returns to a ground state that is measured in an attempt to gain information about the electronic properties of the system. In order to interpret the measurement, one first requires an understanding of the environment in which the excitations take place. Many theories exist which approximate the behavior of electrons in excited systems, and therefore make possible useful interpretation of experimental data. With the advent of accessible computation power, many numerical calculation programs have been developed for the purpose of simulating the electronic structure of molecular systems, in complement to spectroscopic measurements. The following sections introduce the basic theoretical framework required to understand both the electronic structure of molecular systems, as well as the numerical calculation methods used in this work.

3.1. Molecular Orbital Theory

In molecular systems, the description of electronic structure is necessarily more complicated than that of individual atoms. In order to study and work with such systems, an approximation is required known as molecular orbital (MO) theory. This approximation implicitly assumes that a general molecular wave function may exist for a given system, developed through a superposition of the atomic wave functions of the components that make up the system. The molecular wave function is constructed by the linear combination of atomic orbitals (LCAO) method which is governed by several assumptions that define the behavior of the system. Namely, that atomic orbitals overlap to form MOs when in sufficient proximity, orbitals only interact strongly if they are of nearly the same energy, and two interacting orbitals combine to form opposing bonding (occupied) and antibonding (unoccupied) states.

For low-Z molecules which are the focus of this manuscript, the most useful way to describe MOs is by their symmetry, specifically by either σ or π character. To illustrate the formation of σ and π bonding and antibonding orbitals, take the example of the simple molecule ethylene (C_2H_4). The electron configuration of carbon in notation using the primary quantum number (*n*) and the angular momentum quantum number (*l*) is $1s^22s^22p^2$. This configuration possesses orbitals of both *s* and *p* symmetry, the general shapes of which are shown in Fig. 3.1.

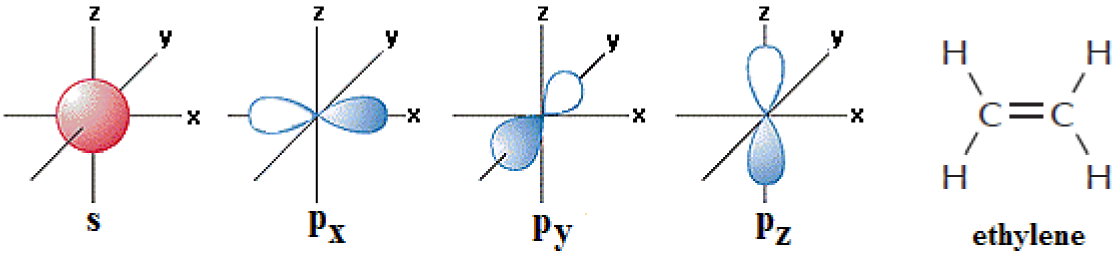

Figure 3.1. Shapes of *s* and *p* type orbital wave functions and the form of the ethylene molecule

p-type orbitals (as well as *d* and *f*) possess lobes with different phases which allow for interference in a constructive or destructive way to form bonding or antibonding orbitals of either π or σ type. Orbitals of each type are given labels according to their relative orientation to the bond axis connecting them. π-bonds are described as those that are antisymmetric in phase with respect to C_2 rotation along the bond axis, and also contain a node along the bond axis. To form an ethylene molecule, a double bond occurs between the two carbon atoms, and single bonds with the peripheral hydrogens. The 2*s* and two of the 2*p* orbitals combine or hybridize to form three sp^2 orbitals oriented along a plane, with one *p* orbital remaining untouched and oriented orthogonal to the plane of the sp^2 orbitals. A π-bond with both bonding and antibonding states (Fig. 3.2) is formed by the untouched p_z orbitals projecting orthogonal to the bond axis which make up one of the two C-C covalent bonds.

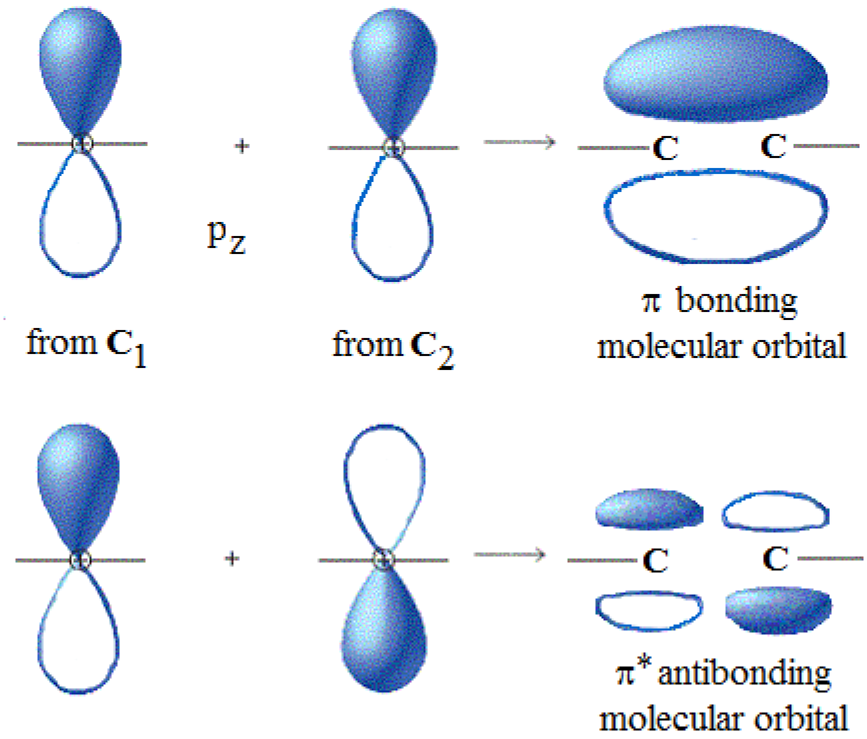

Figure 3.2 Example of π-bonding where constructive and destructive interference create bonding and antibonding orbitals.

The second covalent bond is generated by the sp^2 orbital lying directly along the bond axis, with the other two sp^2 orbitals bonding to the hydrogens. This type of direct bonding is designated as a σ-bond which describes the electron distribution along the bond axis (Fig 3.3).

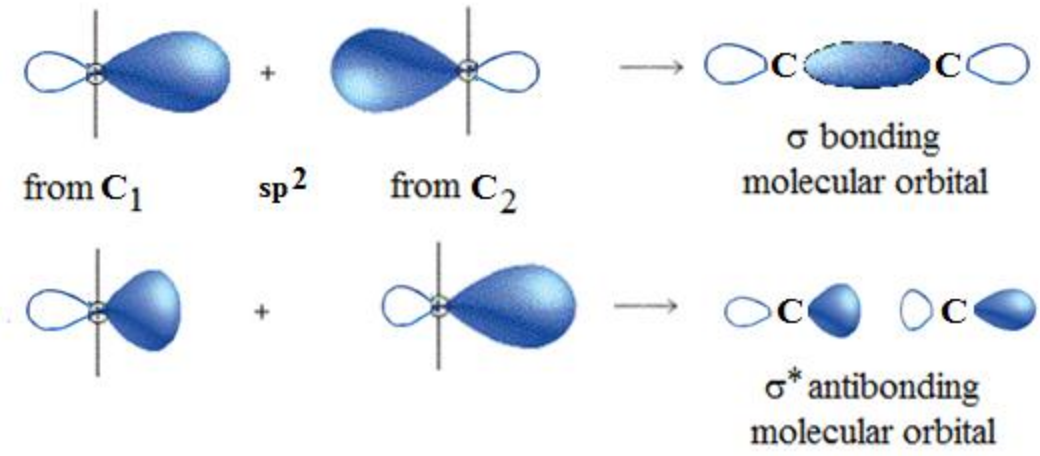

Figure 3.3 Example of σ-bonding through sp^2-type orbitals

For the case of ethylene, the C-C covalent bonds originate from sp^2 orbitals generated from hybridization of 2*s* and 2*p* orbitals, with the 1*s* orbitals remaining localized on the atomic centers and not participating in bonding. This type of hybridized bonding is commonly seen in organics where the C-C interaction generally takes the form of such hybridized bonds containing both *s* and *p* components, with one *p* orbital left untouched to form a π bond. However, the nomenclature remains the same as the naming of the bond type is a product of orientation relative to the bond axis only, and not the orbitals that contribute to it. Therefore, hybridized bonding in the context of MO theory will not be discussed further, and all bonds will be referred to as either σ or π with associated bonding (σ,π) or antibonding (σ*,π*) states in the following discussions.

3.2. Density Functional theory

In general, the electronic structure of matter is extraordinarily complex and consequently impossible to directly calculate for all but the simplest of systems. Density functional theory is one of the common methods that have been employed to successfully approximate the electronic properties of an arbitrarily complicated system. Conceptually simplified, DFT models condensed matter systems as a cloud of electrons which is subject to a potential created by the nuclei. The cloud of electrons is modeled as a density function that describes the distribution of electrons in space. The principle of DFT is then that all properties of the system may be derived from the character of the density function. The end goal of DFT calculations is to find the form of this density function and analyze it to extract the desired electronic properties of the system.

Throughout this work, DFT calculations are used to simulate X-ray spectroscopy measurements and to compute the distribution of molecular orbitals. However, an in depth understanding of the underlying theory of DFT is not a requirement for performing calculations. In the following sections, the basic formulation of DFT is summarized in the context of how electronic properties may be calculated using this theory. This is followed by a short section referencing basis sets which are the starting point for all simulations. Section 3.3 then discusses how calculations were practically performed with the software packages used in this work.

3.2.1 The Hohenberg-Kohn Theorems and Kohn–Sham Equations

The basis of density functional theory began in 1964 with the work of Hohenberg and Kohn [9]. In their report, they bring to light two important proofs which describe the nature of the density function. The first shows unequivocally that the there exists a unique density function for each unique external potential. This means that two systems with differing electronic structure and therefore a different external potential cannot have identical density functions. This therefore indicates that the electron wave functions which make up the density function are also unique for a given potential.

The second proof was more of a development of the method that one would use to find the density function for a given system. The method is the Hohenberg-Kohn Variational Theorem which begins by selecting a candidate density function, with associated electron wave function. Then, it is noted that the energy of a given system must be greater than the ground state energy unless it is in fact the ground state energy. Since there will be only one unique electron wave function associated with the ground state, there is therefore one density functional. Thus, the ground state density may be found by variation of the density function until the system is in the lowest possible energy state.

These proofs provide the theoretical framework for the use of DFT to calculate electronic structure, but do not give any practical insight into how one would actually compute the density functional. This issue was resolved one year later in 1965 by Kohn and Sham who developed the self-consistent field (SCF) method for computing the ground state density [10]. The SCF procedure is in essence an iterative method which allows for calculation of the density functional given an initial set of parameters. The issue with the Hohenberg-Kohn theorems as stated is that the exchange and correlation terms could not be properly modeled, stopping the computation before it had begun. The breakthrough of Kohn and Sham was to treat the electron gas as a system on non-interacting particles with the same ground state density as its fully interacting counterpart. This definition provided an enormous simplification, allowing a set of equations to be derived which describe the density function (1), which is a superposition of the orbital wave functions of the non-interacting particles, the effective potential of the nuclei in the system (2), and a single-particle Schrödinger equation (3). Note in equation (2), the term $v_{xc}(\boldsymbol{r})$ is the exchange correlation functional, defined as the derivative of the exchange-correlation energy with respect to the density function. $v_{ext}(\boldsymbol{r})$ is the external potential due to the positively charged nuclei.

$$\rho(\boldsymbol{r}) = \sum_{i}^{N} \langle \varphi_i(\boldsymbol{r}) | \varphi_i(\boldsymbol{r}) \rangle \tag{1}$$

$$V_{EFF}(\boldsymbol{r}) = v_{ext}(\boldsymbol{r}) + \int \frac{\rho(\boldsymbol{r}')}{|\boldsymbol{r} - \boldsymbol{r}'|} d(\boldsymbol{r}') + v_{xc}(\boldsymbol{r}) \tag{2}$$

$$\left(-\frac{\hbar^2}{2m} \nabla^2 + V_{EFF}[\rho(\boldsymbol{r})] \right) \varphi_i(\boldsymbol{r}) = \varepsilon_i \varphi_i(\boldsymbol{r}) \tag{3}$$

These equations make up the so-called Kohn-Sham equations, where a self-consistent solution to them provides a model of the electronic structure of the system that can be solved for iteratively. A starting model of the density functional provides a value for the effective potential, which can then be used to solve the Schrödinger equation, with the resulting eigenfunctions used to generate a new density functional. The iterative process is simply repeated until the changes in the density and interaction energies are less than predefined convergence criteria, at which time the ground state has been found.

3.2.2. Basis Sets and Exchange-Correlation Functionals

As with any iterative procedure, DFT calculations require an initial input on which to base the density function. For this purpose, basis sets exist which consist of a set of functions that approximate the orbitals of a particular element. These functions approximate the *s, p, d* or *f* character of actual orbitals using combinations of Gaussian type functions to mimic the character of real orbitals as much as possible. Practically, when choosing basis sets for a given system, there is a tradeoff between the relative complexity of the sets used, and therefore increased calculation time, and the accuracy of the results.

In addition to basis sets which give the starting orbitals for the SCF procedure, models of the exchange-correlation functional are required. These functionals model the interaction between electrons in the system (exchange) and the electron interaction with the electronic structure of the surrounding system (correlation). This is particularly important for calculations involving an excitation where a core hole is present which can severely modify the electronic structure. This presents a large difficulty as exchange-correlation interactions are only calculable for a free electron gas, where models for other systems must be derived through simplifications or approximations.

3.3. Electronic Structure Calculations

Throughout this study, numerical calculation programs utilizing DFT were employed to simulate electronic structure. The programs used were StoBe, the Stockholm-Berlin version of deMon [11] and Gaussian03 [12]. These programs are used to simulate electronic structure, as well as X-ray spectroscopy measurements for comparison with experimental results. Gaussian is primarily used for computation of the dipole moments as well as generation of MO isosurfaces for presentation, such as those shown in section 5.1.4. In the following sections, basic details of how calculations were performed using these programs are included. Since plenty of documentation is available for new users, these sections are intended to lend a basic understanding of what is involved in setting up an electronic structure calculation and interpreting the results.

To begin, all calculations require the basic structure or assumed structure of the molecule or lattice to be simulated. In all cases, the first step is to perform a geometry optimization which attempts to find the lowest energy configuration of the structure in question. This step is essential as in nature all stable materials will by default be is the lowest energy state – otherwise their structure shift until such a state is reached. Once an optimization step is complete, all further calculations of properties are done using the lowest-energy configuration.

3.3.1. Simulating NEXAFS spectra with StoBe

X-ray absorption by definition must involve the creation of a core hole, and simulations must take this into account. To model the effect of a screened core hole, the Slater transition state method is used where the excitation step is treated by replacing the core hole by a half core hole, and leaving the unoccupied states empty [13]. This method has been found to more accurately model NEXAFS electronic structure, but it does not provide an accurate absolute energy scale, with simulated spectra requiring additional calibration.

For this work, specific basis sets and exchange-correlation functionals were used which have been found by experience to give accurate results without extreme calculation times. NEXAFS simulations were performed using the StoBe package which implements DFT with both auxiliary and orbital basis sets based on the Huzinaga basis sets originally developed for Hartree-Fock calculations [14]. The auxiliary sets used for geometry optimization - and X-ray excitation where applicable – were triple-ζ plus valence polarization (TZVP) sets [15]. Orbital basis sets derived from the TZVP sets were also used in the calculation. For calculation of absorption spectra, the atomic site undergoing excitation is characterized using the *iii_iglo* orbital basis to obtain a more accurate representation of the relaxation of atomic orbitals during excitation. This basis set is much larger, containing additional terms that provide a better approximation then the sets typically used. Ideally, such a basis set could be applied to all atoms in the system, but the expense in calculation time would become prohibitive. The exchange-correlation functional used in StoBe is based on the generalized gradient approximation, developed by Perdew [16], with the exchange functional by Becke [17]. A listing of the specific basis sets used is shown in the Appendix.

The core-hole is modeled by altering the charge in a specific orbital specified by its energy, and without this modification the core-hole may move to C sites other than the one specified during the calculation. This occurs due to multiple degenerate orbitals present at similar C sites. To alleviate this, equivalent core orbitals of non-excited C atoms were replaced with modified TZVP effective core-hole potentials in order to specify the site of the core hole unambiguously, and thus obtain results from a specific C site with a fixed core-hole. Effective core hole potentials are special basis sets which modify the core level of all non-excited atoms, such that the core hole is fixed at the desired site. Using this method, the oscillator strengths for core level excitations to unoccupied states were computed for each C atom individually, and summed to produce the total spectrum. For comparison with measurements, the simulated spectra were broadened by convolution with Gaussian functions with line width (FWHM) of 0.5 eV up to 290 eV, and then linearly increasing up to 5 eV over the next 10 eV.

3.3.2. Energy Calibration

As mentioned previously, the transition state method provides the most accurate description of NEXAFS spectral features, but is deficient in providing a consistent absolute energy scale. A solution to this issue is provided by the StoBe authors [18] such that a correct absolute energy scale may be calculated. The procedure centers around the fact that the transition state contains a half filled core hole and empty unoccupied states. This does not reflect the true state of an absorption process where the core level contains a full core hole, with an electron promoted to unoccupied states. To account for this, two additional calculations must be performed for each atomic site; a ground state calculation where no excitation occurs, and a fully excited state containing a true core hole. The total energy of the fully excited state is then the energy of the lowest energy transition. Then, with the total energy of the ground state, the true energy of the lowest transition may be computed by the difference between ground and excited states. The energy scale of the transition state spectrum may then be simply shifted such that the lowest energy transition occurs at the appropriate energy. This procedure must be applied to the calculation for each separate site such that when the individual spectra are summed, they are all calibrated to the same absolute energy scale.

3.3.3 Calculating Electronic Structure with GAUSSIAN03

Gaussian03 also employs DFT as a method for calculation, but also offers the ability to use other methods such as Hartree-Fock for the calculation of electronic structure. For this work only the DFT method was used with specific basis sets which have been found to well approximate measured spectra [19,20]. Gaussian uses basis sets and exchange correlation models similar to those used by StoBe. Here the 6-311G basis set developed my McLean and Chandler [21] was used, with the B3LYP exchange-correlation functional which uses Becke's exchange functional [17] and the correlation functional of Lee, Yang, and Parr [22].

The unique property of this program is given by its name, where all basis sets and exchange-correlation functionals are constructed from Gaussian-type functions. This has the advantage of reduced calculation time as compared to StoBe, but at the expense of differing results. Gaussian is also somewhat more user friendly then StoBe, with a graphical interface provided called GaussView. This interface allows for the creation of molecules in any geometry, and includes a large database of common organic molecules, proteins, and other structures. Calculations may be performed with only the interface by simply filling out a series of check lists and boxes which select the various basis sets and parameters, making it very user friendly. In principle, Gaussian has similar functionality to that of StoBe, but the interface does not contain many options by default, such as the calculation of all virtual (unoccupied) states. For this reason, any in depth study does require a working knowledge of various additional key words which may also be input into this interface.

Although this program has potentially large functionality, due to the limitations of the interface it is not well suited to simulation of spectroscopy measurements. As a result, it has only been used in this work to calculate dipole moments and MO isosurfaces, where the details of these calculations are trivial and will not be included here. All measurement simulations shown in this manuscript were computed using StoBe exclusively.

3.4. Synchrotrons and X-ray Radiation

The experiments involving synchrotron light undertaken for this manuscript were performed at the Canadian Light Source (CLS) at the University of Saskatchewan, and the Advanced Light Source (ALS) at Lawrence Berkeley National Laboratory. The beam lines used at these facilities were the Spherical Grating Monochromator (SGM) [23] beam line with the soft X-ray Absorption endstation at the CLS, and the Soft X-ray fluorescence (SXF) endstation at Beam line 8.0.1. at the ALS [24]. Both facilities are active 3rd generation light sources that offer a variety of spectroscopy, scattering, and imaging techniques to a large body of research users.

In order to successfully undertake X-ray spectroscopy experiments at these facilities, an understanding of the operation and function of synchrotron light sources is required. For the purposes of this study however, the focus is on determining electronic and structural properties of organic semiconductor systems, where synchrotrons and X-ray measurement techniques are the tools used to probe such characteristics. Therefore, a highly detailed account of the operation of synchrotron facilities and the production of X-ray light is not included. The following sections detail the basic operation of synchrotron sources and the theory of the measurement techniques used in this manuscript.

3.4.1. Synchrotron Light and Beamlines

In recent years, the construction of 3^{rd} generation synchrotron light sources has made high intensity light of tunable energy readily available for research use. Such light sources produce light by simply accelerating electrons travelling at relativistic speeds around a circular path, or by use of specialized insertion devices which accomplish a similar task. Referring to Fig. 3.4 below, the electron beam is generated by a linear accelerator which in general consists of a metal cathode which emits electrons that are then accelerated through a large potential difference. The electrons gain additional energy and form into bunches through bombardment by radio frequency (RF) radiation at specific intervals. Following acceleration in the linear accelerator, the electron bunches are released into the booster ring which further accelerates them in a circular path using additional RF radiation. The booster ring is a functional requirement of such a facility as accelerating particles to GeV energies using only a linear stage is not economical. Once the electron bunches are accelerated to a predefined target energy dependent on the facility (1.9 GeV at the CLS, and 2.9 GeV at the ALS), they enter the storage ring where they may circulate for several hours, emitting light by manipulation of the beam path. This emitted light is then available for experimentation at beam line hutches containing optical and experimental detection equipment.

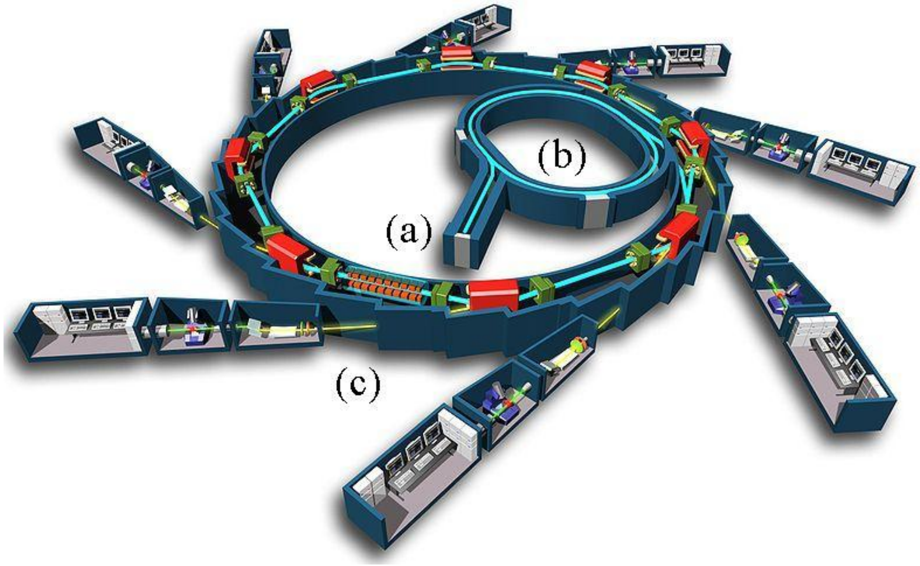

Figure 3.4. General schematic of a synchrotron facility, showing (a) Linear Accelerator Stage, (b) Booster Ring, and (c) Storage Ring with beam line hutches attached. [25]

Manipulation of the electron beam may be accomplished using bending magnets or insertion devices such as wigglers or undulators. Bending magnets serve to simply direct the beam in a circular path, but also provide broad spectrum of lower intensity light which may be directed to experimental endstations. The energy spectrum of available radiation from bend magnets is dependent on the magnetic field they produce - some such as superbend magnets with fields as high as 5 T. Insertion devices are specially designed to produce light of high brightness or with specific properties such as elliptical polarization [26], and are placed on straight portions of the storage ring and are not responsible for directing the electron beam. Two common types of insertion devices are wigglers and undulators which generally consist of arrays of magnets which produce large, spatially periodic magnetic fields perpendicular to the beam path.

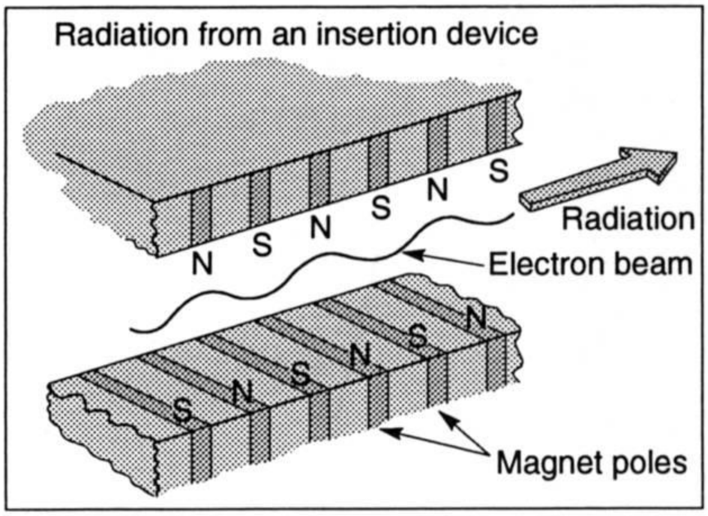

Figure 3.5. Schematic representation of the electron beam path and resulting radiation from an insertion device [27].

The periodic fields cause transverse acceleration of the electrons resulting in a sinusoidal beam path through the device with light emitted at each bend in the path. The light is emitted in directions tangent to beam path, and travels in a tight cone along the mean direction of the unperturbed beam. Both undulators and wigglers produce intense quasi-monochromatic light of variable energy depending on the device parameters. For the case of wigglers, emitted light from each sinusoid period also may be allowed to constructively interfere due to the geometry of the device, creating much higher intensity light which may also be of a specific energy range determined by the strength of the applied magnetic fields.

Once light of a desired energy range is produced, it must be further conditioned by being collimated, monochromatized, and focused before being used for experimentation. These functions are performed by optics contained between the insertion device and the measurement endstation. As an example, below is a schematic of the optics used at Beam line 8.0.1 at the ALS, which employs an undulator as an insertion device to produce soft

X-ray radiation. As shown in the schematic, the beam is conditioned and focused with a series of slits, mirrors and spherical diffraction gratings. The spherical gratings shown below make up the monochromator, which is the central optical component to an X-ray beam line. This device effectively selects the desired X-ray energy and rejects all other energies outside of a narrow bandwidth by controlled diffraction of the incoming radiation.

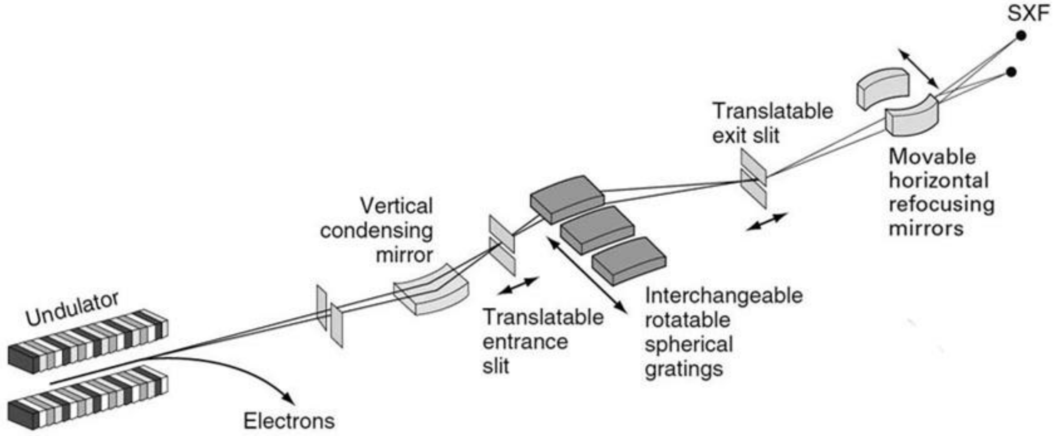

Figure 3.6. Schematic of Beam line 8.0.1, located at the Advanced Light Source, Berkeley, CA [28].

Once the light has been conditioned and an appropriate energy is selected, it enters the experimental endstation. Since the systems studied in this work consist primarily of low-Z elements, only soft X-ray beam lines produce light of the appropriate energy range for measurements (~200 – 2000 eV). Soft X-rays are strongly absorbed by most materials including air, which necessitates that all of the beam line optics and endstation components be situated in high vacuum chambers. The endstation itself typically consists of an apparatus which allows samples to be loaded and maneuvered into the beam path, as well as various measurement devices depending on the function of the beam line. The specific equipment may vary, but for the spectroscopy measurements reported here four main components are required – a nearly transparent gold mesh or photodiode, a specially designed sample plate, a Channeltron detector, and a spectrometer. The detail of specific instrumentation required for the various measurements in this study is further discussed in the following section.

3.4.2. X-ray Spectroscopy Techniques

The primary techniques used in this research to study properties of materials are soft X-ray spectroscopy techniques which employ synchrotron radiation to probe the partial density of states (DOS) of a system. Specifically, they directly measure the energy levels of a system and the probabilities of transitions between those levels to study the underlying electronic structure. The methods used are X-ray Absorption Spectroscopy (XAS) and X-ray Emission Spectroscopy (XES) which are complementary techniques used to examine the unoccupied (antibonding) and occupied (bonding) states of a system, respectively. A specialized form of XAS - angle resolved XAS where the incident angle of the incoming radiation is varied - is also heavily used in this study and is discussed in section 4.3. Both techniques involve absorption of an X-ray photon by a core level electron, but have differing final states dependent on the energy of that photon.

In a simple one-electron picture, if the incoming photon has an energy nearly equal to the binding energy of a core level electron, it may be promoted to unoccupied bound states within the system. Conversely, if the photon energy is much greater than the binding energy, the electron will be promoted to unbound continuum states, and becomes a free particle. Although certain transitions may have higher probability, any electron in a system may be excited provided that the photon driving the excitation has sufficient energy to complete the transition.

X-ray spectroscopy techniques are enormously valuable for studying complex materials because they are element, site, and symmetry selective, which is made possible for two reasons. First, a material undergoing measurement is illuminated by X-ray light of a very narrow energy bandwidth, meaning that only transitions requiring nearly exactly that amount of energy will be possible. Second, the specific binding energies associated with the energy levels of a given element in a material are unique to that element. This means that excitation at the core threshold of one element will occur for a specific energy that is uniquely different from the core threshold of every other element in the sample, and thus a given measurement will not be contaminated with spectral weight from other elements.

Although X-ray spectroscopies are highly selective in this manner, they unfortunately do not give a complete picture of the DOS for a given element. Due to conservation of momentum, not all transitions for which sufficient energy is available are likely or even probable of occurring. The requirement for conservation of momentum is quantified by a set of selection rules that determine which states an electron may be excited into or decay into based on the characteristics of the transition. In general, there are six possible types of transitions that may occur - electric and magnetic dipole, quadrupole, and octupole - but in the interest of brevity only electric dipole transitions will be discussed in detail. Each transition type is defined by the change in momentum associated with that transition, and each has a different probability of occurring with electric dipole transitions by far the most probable. The selection rules themselves are quantified by constraints applied to the changes in quantum numbers between the initial and final states of a transition. Table 3.1 shows the allowed changes in quantum numbers n, the principal quantum number, l, angular momentum, S, total spin, J, total angular momentum and m_j, the projection of total angular momentum for a dipole allowed transition.

Table 3.1. Selection rules for electric dipole allowed transitions.

Quantum Number	Selection Rule for allowed transition
Δn	(no constraints)
Δl	±1
ΔS	0
ΔJ	0, ±1
Δm_j	0, ±1 ; 0 is forbidden if $\Delta J=0$

It should be noted here that although a transition may be forbidden by electric dipole selection rules, it may still occur at a much lower rate with a lower probability through other types of transitions.

These rules have the effect that for a given system, spectroscopy techniques give information only about certain allowed transitions, as opposed to a complete picture of the entire DOS. In the context of this research where organic materials are primarily composed of carbon, XAS spectra will be excitations originating from the carbon 1*s* core level, where an *s* orbital possesses an angular momentum of $l = 0$. Selection rules then dictate that an excited 1*s* electron may be excited through an electric dipole allowed transition into a *p*-orbital which has angular momentum of $l = 1$, satisfying the constraint for the transition of $\Delta l = +1$. Therefore, in the case of carbon, this electron will be excited to unoccupied 2*p* states within the system. This means that C 1*s* XAS measurements probe the nature of 2*p* unoccupied states. Although not discussed here, in principle other transitions into *d* or *f* states through electric quadrupole or octupole transitions are possible, but these would have both extremely low probability and are unbound continuum states in carbon.

3.4.3. XAS and XES

As described above, absorption and emission measurements provide information about the structure of unoccupied and occupied states respectively. Shown below is a graphical representation of the physical process occurring in these two cases.

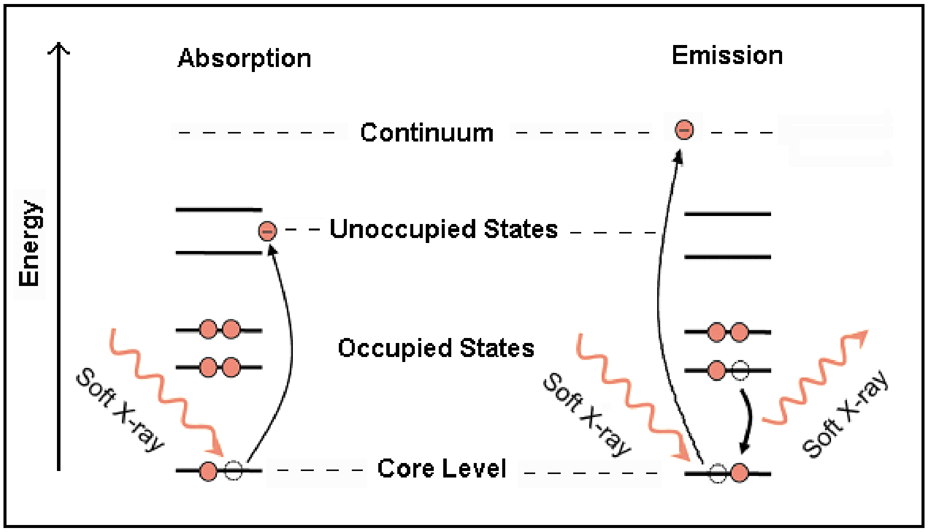

Figure 3.7. Graphical representation of the XAS and XES processes

X-ray absorption functions by first absorption of a photon by a core level electron which causes a transition to unoccupied states, and therefore probes the distribution of bound unoccupied states. The excitation creates a core hole which then must be filled according to selection rules by electrons from either occupied valence states or unoccupied states containing electrons that have been excited. This de-excitation of an electron to fill the core hole can have several possible outcomes, each with a specific probability depending on the element being excited. One possible path is fluorescent photon emission where the electron decay releases a high energy photon which may either leave the sample entirely or be absorbed by a valence electron, infusing it with a large amount of energy. An electron which absorbs this secondary photon now has sufficient energy to easily overcome the work function of the sample and may escape if near the surface, leaving the sample an Auger electron. The second path involves non-radiative energy transfer between electrons through collisions. During the decay to fill the core hole, the electron may transfer energy to other valence electrons through collisions as opposed to emitting a photon, depositing enough energy such that they may also escape as Auger electrons. These two processes give rise to two possible measurement methods: measurement of the ejected photons from radiative decays, or collection of the Auger electrons. Depending on the system in question, one decay path may occur preferentially and will therefore be more suitable for measurements. In the case of carbon, it exhibits a relatively low fluorescence yield which is typical for low-Z elements [29], meaning that collection of Auger electrons will give a much better representation of the DOS with a better signal-to-noise ratio. The decay products can be simply counted by instruments and cross referenced with incident excitation energy to obtain the energy locations of available unoccupied states, as well as the relative probability of transitions to those states occurring.

X-ray Emission measurements are photon in/photon out measurements that commonly occur in two main flavours, non-resonant X-ray emission (NXES), and resonant inelastic X-ray scattering (RIXS). RIXS measurements were not performed for the materials in this study, and this technique will not be discussed further. All other references to ‘XES’ therefore are referring to the non-resonant case. XES is similar to absorption in that the initial step is absorption of an X-ray photon by a core level electron, but in this case the

X-ray energy is much greater than that required for transitions to bound states, and the electron is excited as a photoelectron to unbound continuum states. The core hole may be filled by any other electron which obeys the required selection rules, but the decay of interest is that of a valence electron. In the case of carbon, since the core *1s* level is to be filled, only *2p* electrons may decay. This decay produces a photon of energy equivalent to the energy separation between the valence and core level states, making this measurement a probe of the occupied states within a system. The resultant photons may then be counted similarly to the XAS case, but here a spectrometer is used to collect only those photons within a fixed energy range that originate from valence state decay. However, as mentioned in the previous section, the probability of fluorescence photon emission is considerably lower than that of Auger electron emission, meaning that XES suffers from the same low yield deficiency as XAS fluorescence detection. This is avoided in the case of XES by illuminating the sample with a much higher photon flux such that many more core holes are created then otherwise. This is accomplished by simply widening the exit slit on the monochromator which allows photons to enter the sample chamber. By creating many more core holes, the probability of fluorescence decay is greatly enhanced, but at the cost of lower energy resolution due to the widened exit slits. Therefore, XES measurements are plagued by much lower resolution then XAS, and in the energy range to excite the core level of carbon, can often cause a smearing of fine spectral features which then cannot be identified without the aid of calculations.

As a short note on nomenclature used for XES spectra, which historically uses X-ray notation, defining the transition in question by the core level from which the excitation occurs. This notation uses a capital letter to indicate the principle quantum number, and a subscript indicating the total angular momentum of that level. Notation for all transitions is not relevant for this study, but excitation from the 1*s* core level corresponds to the capital letter *K*. In the case of emission measurements, an additional identifier is added which defines where the electron that fills the core hole originates from. For a *1s* core hole in carbon, the core hole must be filled by a *2p* electron, with the notation '$K\alpha_x$' where 'x' is either 1 or 2 denoting a transition from either the $2p_{1/2}$ or $2p_{3/2}$ levels, respectively. In the context of this manuscript, only excitations from the C 1*s* level have been measured, meaning all spectra are due to *K*-shell excitations, with all emission measurements therefore denoted $K\alpha$.

4. Experimental

In the following sections, the relevant sample preparation and measurement techniques used in this study are discussed. This includes thin film sample preparation using spin coating, X-ray spectroscopy techniques, and some additional practical considerations for X-ray spectroscopy measurements. Throughout this manuscript X-ray spectroscopy collectively refers to the two complementary techniques of XAS and XES which probe the local partial DOS of a material. Additionally, angle resolved NEXAFS was used, which is a special sub-category of XAS measurement with specific application to probing molecular film structure. Although XAS and NEXAFS refer to the same type of excitation, to avoid confusion 'NEXAFS' will only be used when exclusively discussing angle resolved measurements. The theoretical aspects of these techniques have been discussed above, and this section deals with the practical aspects of the measurements themselves that must be considered in order to collect meaningful data.

4.1. Sample Preparation

To produce samples for this study, a spin coater (Fig. 4.1) was used to produce uniform thin films suitable for spectroscopy measurements. Spin coating is one of the most cost effective ways to quickly and easily create thin film samples of organic materials, provided they are soluble. This requires only the spin coater apparatus, solvents, and suitable materials to be deposited as thin films.

Figure 4.1. Image of spin coater equipment with nitrogen source attached.

This spin coater system is a single wafer spin processor which operates simply by securing a small substrate to a rotating stage using a vacuum, and then rotating the stage at a high speed while simultaneously depositing an organic material in solution directly onto the substrate. The substrate is held in place as it is spun by a vacuum generated by either an external vacuum source, or as in this case using a compressed gas such as nitrogen and a venturi-action vacuum generator. The solution must first be premixed at the desired concentration using a suitable solvent and deposited carefully using a syringe.

This method produces a uniform film of a thickness which can vary from 10 nm to 1 μm depending on the rotation speed used, measured in revolutions per minute, and the concentration of the solution. Spin coating allows the dissolved material to take a self-organized crystal structure, the morphology of which is dependent on the processing parameters such as substrate symmetry, rotation speed, solvent, substrate temperature, solution temperature, rotation time and drying time, and drying atmosphere. Spin coated films are also highly reproducible provided the same processing parameters are used for successive samples.

For the two material systems included in this study, all thin film samples were produced using the spin coater, but with a higher solution concentration then is typical which is more suitable for spectroscopy measurements as opposed to actual device fabrication. In the case of device fabrication, one must be very careful to finely control the spin coating parameters to produce an optimum film, which is in itself an in depth study for each material. Additional procedures may also be implemented to optimize thin film structure such as spin coating under inert or solvent saturated atmosphere [30], annealing, or other esoteric drying methods [31].

For spectroscopic measurements, powder PCBM was purchased from Sigma-Aldrich and was measured by pressing the powder into freshly scraped indium foil. The spin-coated films of PCBM were fabricated on clean SiO_2(100) substrates using approximately 1 mL of solution per film of 0.5 % by weight of PCBM (Sigma-Aldrich) with chloroform solvent. The samples were spun at 1200 rpm for 30 seconds. Immediately following the spin casting process, the films were capped with a 5 nm layer of Au by vapor deposition to prevent film degradation due to extended air exposure. This effectively created a buried layer of PCBM which would not be subject to atmospheric contamination from air or water vapor prior to measurement.

Powder samples of the four anthracene-based organic semiconductors were obtained from collaborators at the Department of Chemistry at Korea University, South Korea. Spin-coated films were fabricated similarly on SiO_2(100) substrates using approximately 1 mL of solution of 1 % by weight of material with chloroform. The samples were spun at 2000 rpm for 30 seconds, and no further annealing or post processing was performed.

4.2. TEY and TFY

As mentioned previously, when performing XAS measurements two different decay products are commonly detected – either fluorescence photons or Auger electrons. The method which collects the ejected electrons is termed Total Electron Yield (TEY). This requires a sample mount equipped with an ammeter capable of nA measurement through a connection to ground. When Auger electrons are ejected from the sample, they carry away a net negative charge, leaving a net positive charge on the sample. Charge then flows through the ground connection to neutralize the sample, and the ammeter simply measures the total current that flows over a given amount of time. This technique is best suited for low-Z elements which have a comparatively high electron yield, and was therefore the primary XAS technique used in this study. TEY is also preferentially suited for those samples that are quite thin (~50nm), such as organic thin films. This is because TEY is inherently highly surface sensitive due to the short mean free path of electrons in solids. In order to be counted, an excited electron must be able to escape the sample, making TEY measurements a description of the partial DOS of only the top 2-10 nm of the sample [32].

One may also measure the Total Fluorescence Yield (TFY) which uses a Channeltron fluorescence detector to count escaped photons. The Channeltron detects photons by the electron cascade method, and is also equipped with a mesh exhibiting a strong positive bias voltage to prevent escaping electrons from entering the counter. This method is more bulk sensitive then TEY due to the longer mean free path of photons in solids, and probes the electronic structure up to a sample depth of ~100 nm when using soft X-rays [32]. For transition elements and higher-Z elements, production of fluorescence photons is much more probable compared to Auger yield, and this technique is used to great effect in this case, and is particularly well suited for probing trace elements in dilute samples.

4.3. Angle Resolved NEXAFS

Angle-resolved measurements are a particular class of XAS measurements which take advantage of the polarized nature of synchrotron light. These measurements can be used to determine the average orientation of complicated molecules on surfaces. This has been shown to be successful in many published works for organic semiconductors such as pentacene and poly(3-hexylthiophene) (P3HT) [33], or the liquid crystal poly(biphenyl dianhydride-*p*-phenlenediamine) (BPDA-PDA) [34].

The resonances observed in molecular XAS spectra arise from dipole allowed transitions between 1*s* core orbitals and their antibonding π* or σ* states. π* resonances are lower in energy and comprise the sharp edge features below the ionization potential (IP), representing transitions to bound states. σ* resonances are broad, higher energy features above the IP representing transitions to unbound states in the continuum [35]. Both π* and σ* states arise from covalent bonds between atoms in a molecule, and have a fixed spatial orientation relative to the substrate in the case of a thin film.

This is most easily visualized by example using a benzene ring consisting of six carbon atoms aromatically bonded in a ring (Fig. 4.2). Aromatic carbon structures are common in organic molecules, and present distinct sharp π* features in X-ray spectra, making them ideal for this application. The π*-antibonding states result from two C 2*p* orbitals which project orthogonal to the plane of the ring in the same orientation as the π-bonds themselves. The σ* states result from a hybridization of the *1s* and *2p* orbitals, and are localized in the plane of the ring along the bond axis between each pair of carbon atoms.

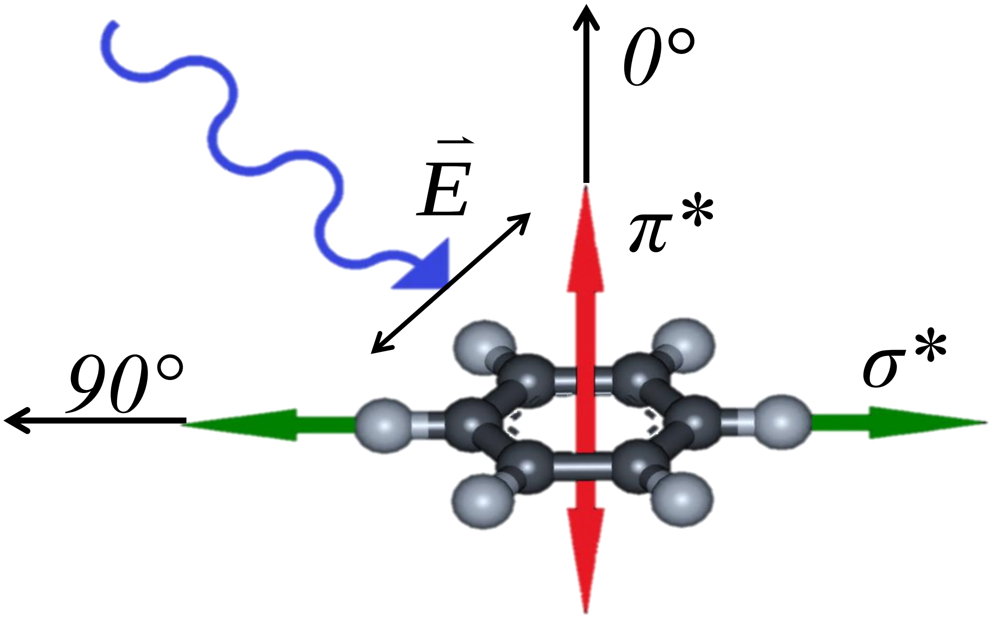

Figure 4.2. Schematic representation of the directionality of π* and σ* states for a benzene ring

When such a structure is resonantly excited, the observed absorption cross section is dependent on the projection of the X-ray polarization vector onto the final state orbitals involved in the transition [36]. The mathematical description of this relationship is rigorously shown by Stöhr [35,36], and only a general description of the function of the technique is presented here. Practically, this means that linearly polarized radiation incident parallel to the plane of the ring (from the 90° direction in Fig. 4.2) will preferentially excite core electrons into π* states, resulting in a sharp, high intensity π* features in the absorption spectra. Conversely, if the angle of incidence is perfectly orthogonal to the plane of the ring (0°), the σ* states will be preferentially excited, and the π* absorption cross section is minimized. Due to this phenomenon, the relative orientation of π-bonds with respect to the substrate may be determined by examining the changes in intensity of π* features with changing angles of incidence. This angular dependence is also visible in σ* features, but these are often more difficult to analyze for large molecules because these broad features tend to be a convolution of resonances from different molecular constituents that cannot easily be separated. The use of this method to determine molecular structure is illustrated below in Fig. 4.3 which shows angle resolved measurements for highly ordered pyrolytic graphite (HOPG). From the measurements, it is clear that at 0° incidence the π* feature is almost completely suppressed, which immediately confirms qualitatively that the plane of the graphite sheets is nearly parallel to the plane of the substrate.

In the context of organic semiconductors as discussed earlier, charge transport properties of these materials highly depend on their structural orientation and degree of π-orbital overlap. Using angle-resolved NEXAFS, the orientation of π and σ bonds and therefore the orientation of the molecules with respect to each other can in principle be determined. It should also be noted here that this technique is made possible in organic materials because in an absorption event, the final state orbitals of the transition must be *2p* states due to selection rules. Therefore, all observed resonances in a C *1s* XAS spectrum are subject to incident angle orientation dependence.

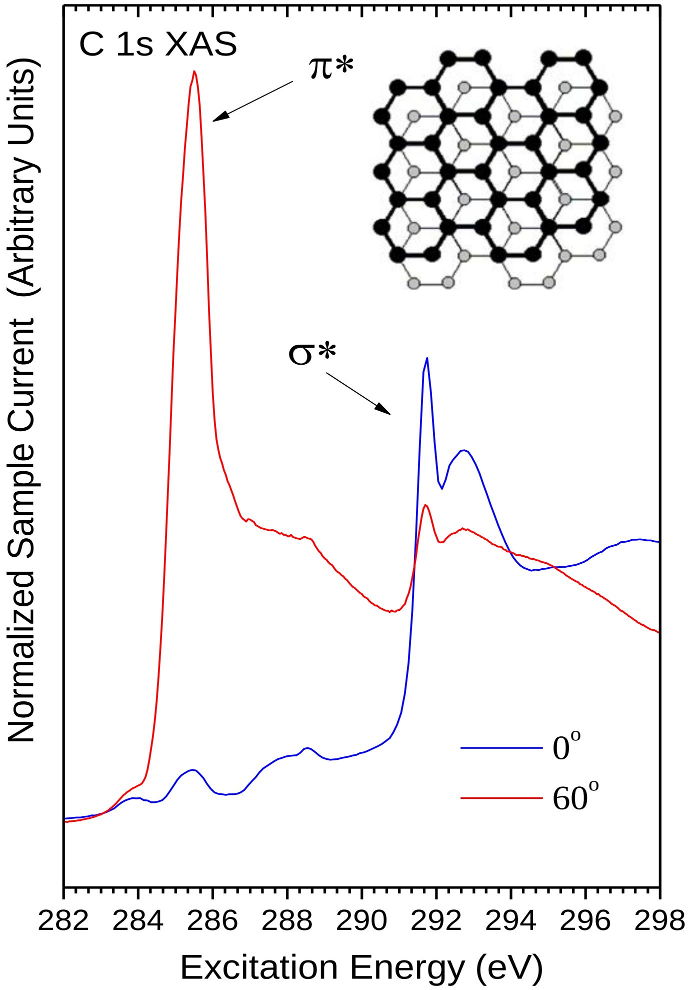

Figure 4.3. Angle-resolved NEXAFS measurements of HOPG for normal and near grazing incidence.

4.4. Energy Calibration and Normalization

Due to the complexity of synchrotron facilities, many factors are at work during a spectroscopic measurement which can affect or disrupt the results in an unknown way. One source of error that is present for every measurement at an experimental beam line is the absolute energy calibration of the monochromator. One of the main strengths of synchrotron sources is the fine tunability of the X-ray energy, but in practice the actual energy of the photons that enter the monochromator cannot be determined directly, introducing unavoidable uncertainty. The X-ray energy is determined mathematically through the relationships between various parameters of the optical components - such as the positions of the diffraction gratings in the monochromator - which themselves have some inherent uncertainty. In principle, if the exact location of all optical and beam line components was precisely known, there would be no need for any post processing calibration. However this is not the case and throughout the course of an experiment the calculated energy of the photons entering the sample chamber departs from the actual value – from ~0.5 eV to as much as 50 eV depending on the beam line and energy range in question.

This is accounted for through the use of calibration samples with highly repeatable spectra and well-defined resonance peaks with accepted energy locations. An absolute calibration is performed by first simply measuring the calibration sample to observe the energy shift of its resonances relative to the accepted values. For this study, the standard calibration sample for C 1*s* measurements, HOPG, was used with the sharp π* feature located at 285.5 eV used for calibration. For C Kα XES measurements, HOPG is also used, with the sharp emission feature located at 277 eV. All other spectra taken in the same experimental run are simply hard shifted into agreement with accepted values. It should be noted that this procedure assumes that the movement of the monochromator and beam line optics is reproducible over a small energy range, meaning that it is only valid provided that all of the spectra to be calibrated were measured over the same energy range, and without scanning the energy over a different range in between measurements. This method of hard shifting also requires that the shift is relatively small (~1 eV) and that the energy range of the entire measurement is not excessively long. Due to the complexity of beam line optics, the relationship between photon energy and instrumentation parameters is highly non-linear. This means that if large shifts over long energy ranges are required, shifting each data point linearly by the same amount is unreasonable, as different points require slightly different shifts. To obtain a correct calibration in this case, a mathematical procedure should be applied to compute the required shift for each data point separately.

Apart from energy calibration, all XAS spectra are inherently subject to variations in intensity of the incoming X-rays, which arise from electron beam instabilities in the storage ring or variations in the beam line optics. Such instabilities have the effect of generating artifacts in experimental spectra which can be mistaken for or wash out true spectral features. This problem is accounted for at the both the SGM and SXF beam lines through the use of a nearly transparent gold mesh which is placed just before the sample chamber. Gold is used for this purpose in soft X-ray beam lines as it possesses very low absorption coefficients in this energy range. When illuminated with synchrotron light, the photocurrent produced in the mesh as a function of incident photon energy provides a measurement of the relative intensity of photons entering the sample chamber. In this way, a simultaneous measurement of the beam current, given the symbol I_o, is taken during every measurement to quantify any fluctuations in photon intensity. Any artifacts produced by such fluctuations are then removed from the measurements during post processing by simply dividing the measured spectra by I_o.

For the case of carbon, however, the situation is somewhat more complex. Although the gold mesh is situated in high vacuum, it is the beam line component that is closest to the sample chamber. Of all beam line components, the sample chamber is most susceptible to contamination as it has direct contact with the samples to be measured. During a measurement, samples are illuminated with an intense beam of X-rays which deposits large amounts of energy in the sample. This can cause radiation damage which is discussed below, as well as flash heating of the sample which can cause outgassing. Due to the proximity of the gold mesh to the sample chamber, it may be easily contaminated with trace elements which may have absorption resonances within the energy range of interest. If this is the case, then the mesh itself may absorb some of the incoming photon flux, causing artifacts in the I_o signal, and potentially erroneous normalization. This has proven to be a problem for carbon in particular as this element is ubiquitous in our environment and impossible to keep out of the vacuum chambers and off of the mesh. The practical result is that some of the X-rays incident on the Au mesh will be absorbed by the carbon contaminant adsorbed onto the mesh. Therefore, the beam current measured by the mesh is not an accurate representation of the photon intensity actually reaching the sample, and is inappropriate for normalization. At the SGM beam line where NEXAFS measurements used in this study were taken, the beam line personnel have implemented a solution to this problem for carbon XAS. This solution makes use of a photodiode which is situated behind the sample plate within the sample chamber, in the beam path. Due to this geometry, the photodiode directly measures the photon intensity that actually enters the chamber and would strike the sample. The only downfall of this arrangement is that a photodiode measurement may not be taken simultaneously with the measurement, and therefore it does not directly account for any beam instabilities that may occur during the measurement itself.

Although this drawback exists, through experience it is clear that the photodiode method provides much better results even with the risk of introducing artifacts that would otherwise not be present. This is illustrated in Fig. 4.4 which presents a C 1*s* XAS measurement of the *n*-type organic semiconductor N,N-1H,1Herfluorobutyl dicyanoperylenediimide (PDIF-CN2) taken at the SGM beam line. This material is a complex polymer and displays rich electronic structure with many small features that can be easily distorted by instability artifacts. The center panel shows the TEY spectrum normalized using the I_o signal collected simultaneously. It is clear from the figure that this normalization severely distorts the spectrum with unwanted artifacts, making it completely unusable. In contrast, the bottom panel shows the same spectrum normalized using the photodiode measured beam current, with a correctly normalized spectrum as the result.

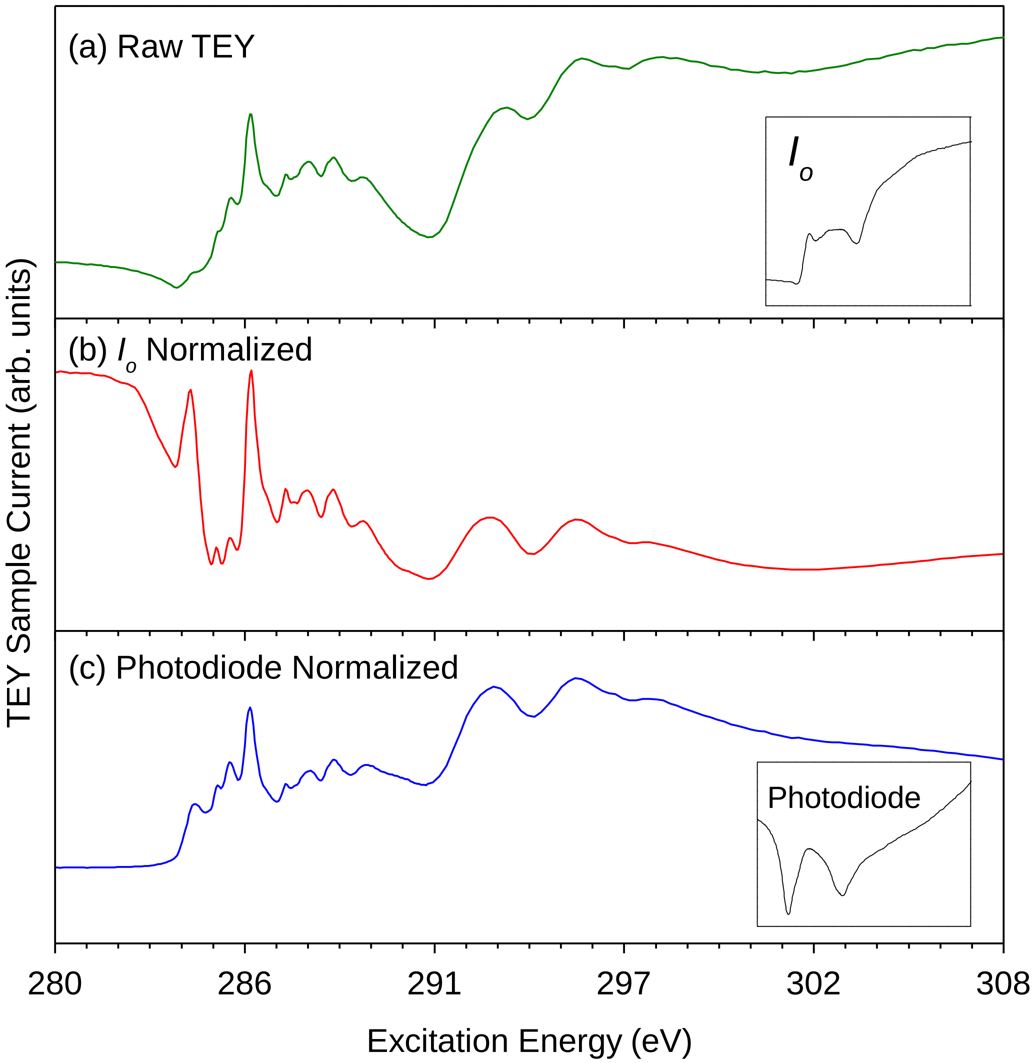

Figure 4.4. (a) The raw TEY signal of PDIF-CN2 with the simultaneously measured I_o signal in the insert. (b) The I_o normalized TEY signal. Note the severe distortions to the spectrum with the resonances barely recognizable. (c) The same spectrum normalized with the photodiode beam current, with the photodiode beam current shown in the inset.

4.5. Radiation Damage

Apart from energy calibration and normalization procedures, the other main concern particularly relevant for organic materials is radiation damage during any type of spectroscopy measurement that illuminates a sample with high energy light. Severe radiation damage in organic materials is a well-known challenge when using soft X-ray radiation, and has been studied for various materials in thin films [37-39]. When a sample is irradiated during a measurement, electron excitations occur throughout the material, and also a large heat load is deposited on the sample. The increased heat load can have the effect of violent outgassing of a powder or film sample depending on the material, which will disrupt film structure and break chemical bonds in the material, as well as contaminate the vacuum chamber. Due to this, cryo-cooling is often implemented to cool the sample to liquid nitrogen or helium temperatures in order to reduce damage, but this is not always available or appropriate for every sample. Beyond excessive heat, the primary source of damage is the ionization of atoms or constituents in a molecule, which is particularly prevalent in organics due to the low ionization potential of ~290 eV for most materials. Such ionization can cause broken bonds and separation of functional groups from the main molecule, causing new bond formations or generation of entirely new chemical species [39]. Also, the radiation dose that a given material can sustain without significant damage varies greatly, and is very difficult to predict.

From a spectroscopy point of view, radiation damage results in a change in spectral features during the course of an experiment, or even during the course of a single measurement. This can greatly affect results when multiple measurements are taken of the same sample, such as in the case of NEXAFS. To examine the effect of radiation damage, each new material should be tested for radiation damage at the start of an experimental run by several repeated absorption measurements of the near-edge region on the same sample spot. If significant radiation damage occurs, successive measurements will reveal changes in spectral features such as variations in intensity or changes in the number or location of features. As a general precaution, successive measurements taken of the same sample are always taken at different physical locations on the sample to minimize the damage as much as possible.

At the CLS, the SGM beam line has recently implemented a new system which allows the entire energy range of a measurement (typically 20 – 30 eV for carbon) to be scanned over in 10 – 20 seconds. This fast scanning method is preferable to the typical form of measurement where the sample is illuminated at each energy step for a dwell time of 1 s. For a typical measurement range of 20 eV at 0.l eV steps, a sample would undergo ~200 s of constant high energy X-ray bombardment. Clearly, this type of system is ideal for organic materials to reduce radiation damage without the need for cooling to cryogenic temperatures.

5. Results and Discussion

5.1. Anthracene-based Organic Semiconductors

As discussed earlier, small molecule p-type organic semiconductors have been used to produce OTFTs showing typical hole mobilities as high as 1 cm^2/Vs [1]. However, the achievement of this performance requires complex fabrication procedures involving vapor deposition in vacuum or inert atmosphere similar to conventional inorganic materials, which severely limits the application to low cost, large scale processing. In answer to these difficulties, organic semiconductors soluble in common organic solvents may be used with solution processing techniques such as spin coating or drop casting. These methods are better suited to large scale processing, but the quality of films they produce is typically inferior, displaying disordered molecular arrangements with insufficient crystallization. This can be alleviated somewhat through the use of post processing techniques such as annealing, but this requirement further increases the complexity and somewhat nullifies the low cost advantage of solution based approaches.

Due to these difficulties, much work has focused on design of new materials which intrinsically possess desirable properties such as a propensity to crystallize in thin films. To this end, a class of novel anthracene based materials has been recently synthesized that display good film forming properties and high charge carrier mobility (0.240 cm^2/Vs for OTFT) when spin cast without the need for any post processing [8,40]. A set of four such anthracene-based materials are the subject of this study, and are shown in Fig. 5.1. All four of these materials are very similar in structure, differing only in the specific geometry of the thiophene groups and additional alkyl chains on two of the four. As a short note on the naming convention used, these molecules are given short names where the prefix ‘HB’ indicates attached alkyl chains, and the suffix ‘THT’ refers to an ethynyl bridge between the thiophene and anthracene, with ‘HT’ being a simple single bond.

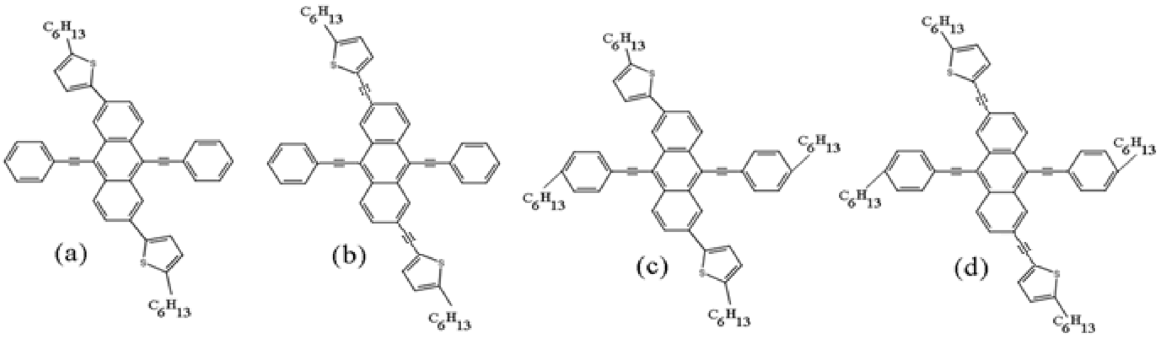

Figure 5.1. Schematic representations of the four anthracene-based materials, (a) B-ant-HT, (b) B-ant-THT, (c) HB-ant-HT, and (d) HB-ant-THT. Note the structural similarities between them.

Shortly following their fabrication, thin films of these materials were created using SiO_2 substrates, but also with the inclusion of octadecyltrichlorosilane (OTS) as a self-assembled monolayer (SAM) coating on the substrate. SAM materials are often used as a substrate treatment in an attempt to enhance the crystalline structure and performance of semiconductors deposited on top of them [41]. The resulting thin films were characterized using X-ray Diffraction (XRD), cyclic voltammetry (CV), UV-Vis spectroscopy, and Atomic Force microscopy (AFM), and also used to fabricate OTFT devices where the I-V characteristic was measured.

XRD results showed clear diffraction peaks indicating the presence of structural ordering. In particular for B-ant-THT and HB-ant-THT, a clear (100) diffraction peak indicates two dimensional structure with most of the crystallites oriented along the (100) axis in plane [40]. Similar results were found for B-ant-HT and HB-ant-HT, with the latter displaying a much more ordered structure, shown in Fig. 5.2.

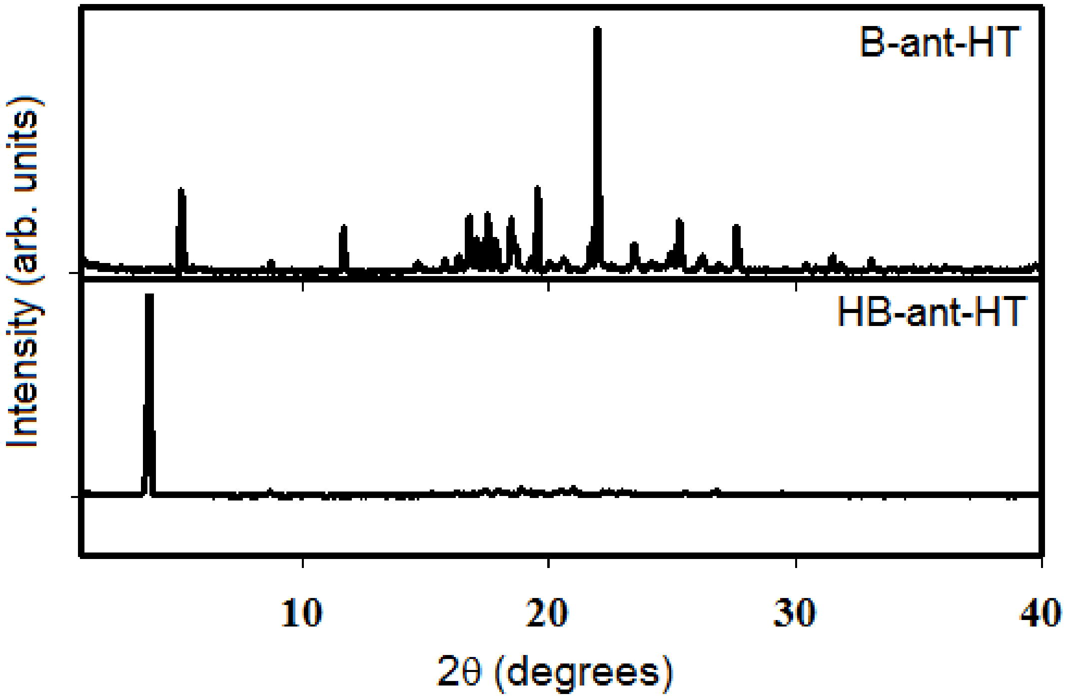

Figure 5.2. XRD measurements of B-ant-HT and HB-ant-HT thin films fabricated at room temperature without additional annealing. HB-ant-HT shows only one sharp (100) peak, indicating a high degree of structural order. Measurements taken by collaborators at the 8C1 and 3C2 beamlines, Pohang Accelerator Laboratory, South Korea.

From these results, the vertical *d*-spacing is found, and the general orientation of the plane of the anthracene core is determined to be nearly normal to the substrate with a slight tilt angle. Similar upright structures have been observed for related acene derivatives [42-44], and in general such materials tend to form herringbone or slipped stack type crystal structures (Fig 5.3) [45-47]. Such other materials also display relatively high charge carrier mobility, but in all cases good performance is only obtained for measurements performed in vacuum or with additional post-processing.

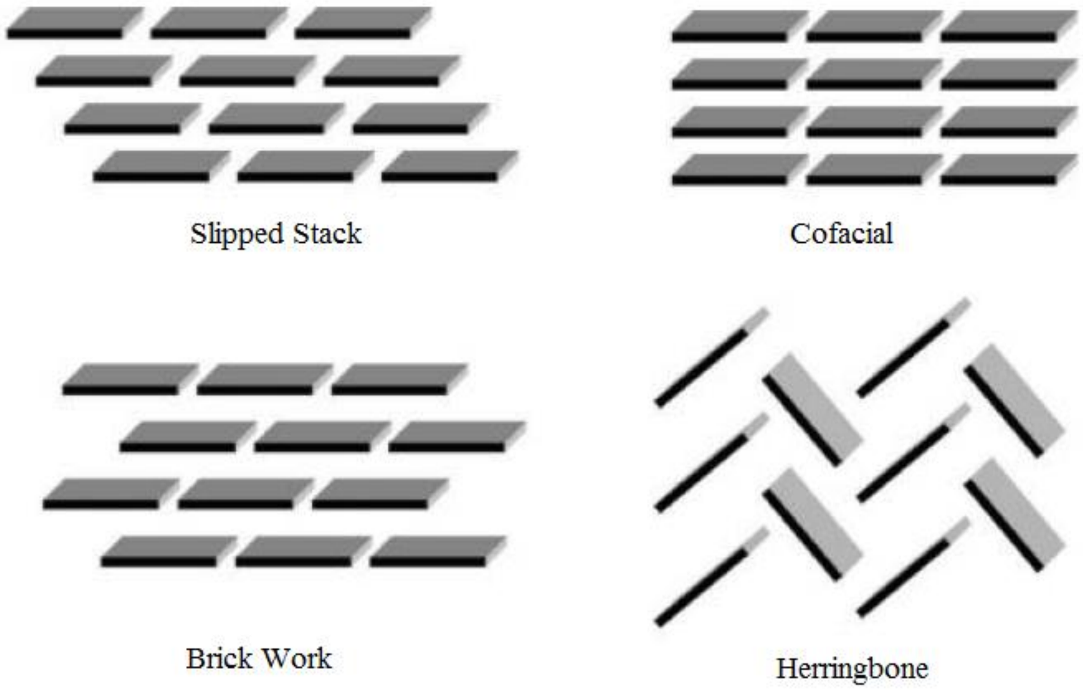

Slipped Stack

Cofacial

Brick Work

Herringbone

Figure 5.3. Common stacking structures exhibited by functionalized acenes [46].

For the remainder of this section, the results of previous studies are used in conjunction with new measurements to determine the thin film stacking structure of these materials. The following section is a short discussion about the effect of molecular stacking structure on charge carrier mobility. From there, the molecular stacking structure of these materials in spin coated films is probed using angle resolved NEXAFS. The UV-Vis and CV measurements were used to determine the HOMO and LUMO levels of these materials, and compute the energy gap. The gap may also be determined using C 1*s* XAS and C $K\alpha$ XES measurements, which is detailed in section 5.1.5 with the literature results compared to those found in this work. DFT calculations were performed to simulate NEXAFS measurements in order to de-convolute the spectra and identify which resonances originate from each molecular constituent, as well as identify the physical locations of the HOMO and LUMO on each molecule.

5.1.1. Thin Film Structure and Charge Carrier Mobility

The present research focuses on optimization of characteristics of existing materials by studying electronic structure and thin film structure. The thin film structure in particular heavily affects charge carrier transport in organic materials. This is because organic materials are typically polycrystalline or completely disordered, lacking a highly ordered structure as is typical of inorganic semiconductors where charge carriers move via band transport. In organic materials, conduction methods are still not well understood, with several different models existing that apply more or less accurately depending on the material structure in question. Generally, charge carrier conduction occurs not through classical band transport but through hopping between molecular orbitals which can in some cases be approximated as bands when they are sufficiently energy degenerate and delocalized throughout a molecular solid [7]. The molecular orbitals of any given molecule that govern the carrier transport are the HOMO and the LUMO, which are usually localized on a specific portion of a large molecule in the form of bonding π and antibonding π^* states, respectively, originating from π-type C 2*p* bonds. In order for band like transport to occur, the crystal structure of an organic material must be organized such that HOMO/LUMO states of neighbouring molecules overlap (conjugate) sufficiently to create a band-like delocalization of orbitals across the solid. It should be noted here that due to this requirement, inter- and intra-molecular mobility generally vary greatly, and good conduction usually only occurs along certain paths where delocalization and conjugation are maximized. This means that materials with the highest observed mobility are typically those with ordered crystal structures, exhibiting high π-π interaction between molecules. However, as pointed out by Brédas *et. al.* [48], MO overlap between neighbouring molecules does not necessarily indicate that those orbitals are sufficiently coupled to allow charge hopping. In order to properly quantify the interaction, both the degree of overlap and the phase relationship of the orbitals must be considered. Therefore, an understanding of the precise nature of π-π interaction, and not merely the presence of overlap, must be considered in the study of materials for high mobility applications.

In addition to the requirement for π-interaction and charge transfer between molecules, charge carriers in a device must be transferred across a disordered polycrystalline landscape. Presently, two families of transport models exist to describe such conduction, variable range hopping (VRH) and multiple trapping and release (MTR) [33]. VRH type models have been found to be more appropriate for disordered systems, and do not well model polycrystalline or crystalline materials. In this model charge transport occurs through hopping between localized states, and probability of such a hopping event is determined by the energy difference and physical proximity of the states involved in the transition. The MTR model treats polycrystalline materials by dividing the DOS into mobile and trap states [49]. Trap states are generated by impurities such as grain boundaries between areas of different crystal structure, and charge carriers that enter these states are bound in the local area, immobile. Mobile states are then those that are sufficiently delocalized across the material to allow charge carriers to flow. When free charge carriers are present in the material, they will fill the low lying immobile trap states first, creating a threshold of charge carrier density termed the mobility edge [33]. Until the density of free charge carriers reaches the mobility edge where mobile states begin to fill, no conduction will occur across the material.

It is clear that in order to achieve a complete picture of the charge transport properties of a given material, many factors must be considered; from the fine structural properties of the molecules themselves, up to the morphology of bulk thin films. For this work, the focus is on the fine structure of the molecules themselves, and how this allows for orbital overlap and charge conduction. A complete study of film morphology and grain character would be required to further explore the structure, using additional characterization measurements such as surface science techniques which have not been performed.

5.1.2. Angle Resolved C 1*s* NEXAFS

Fig. 5.4 displays angle resolved NEXAFS measurements of thin films of the four anthracene-based materials. Of the four, only two show evidence of high molecular order. Both HB-ant-HT and HB-ant-THT show clear polarization dependence in π* resonances centered around 285 eV, with the intensity showing a general decrease with increasing angle of incidence. The other two materials, B-ant-HT and B-ant-THT, show only minor variations in π* intensity as the incident angle is varied, indicating that the local structure is largely amorphous. This is in contradiction to the XRD results mentioned previously which indicated an ordered structure for all materials, but this is presumed to be due to the use of OTS as a SAM which increased molecular ordering in those samples. No such SAM was used in this case as the film forming properties of the molecules themselves was of interest without external aids.

The two materials which display evidence of ordered structure are those with additional alkyl chains. This directly indicates that the attachment of this group induces order in the films. Looking more closely, the precise nature of the polarization dependence is different for the two molecules, with HB-ant-THT showing a consist loss of intensity with increasing angle, but HB-ant-HT displays a minimum at 60°. Additional polarization dependence is observed in the sharp peak located at 288.5 eV, which follows the opposite trend as the lower lying π* states, increasing in intensity for decreasing incident angle. The difference between HB-ant-HT and its structurally similar partner, HB-ant-THT, is the attachment of the thiophene groups to the anthracene core. This slight geometry modification is then the source of the different film structures these materials exhibit.

Without further analysis, some qualitative insight may still be gained about the nature of the stacking structure these materials exhibit. The π* feature at 285 eV is due to a convolution of resonances originating from the anthracene, benzene, and thiophene groups (shown in the following section) which are all aromatic structures typically possessing unoccupied states in this energy range. From DFT geometry optimization, the anthracene core and thiophene groups are roughly planar, meaning that their π* states project out along nearly the same vector. The attached benzene rings are oriented with the ring planes at a slight angle relative to the plane of the anthracene core. Given their comparative size, the majority of the intensity in the 285 eV feature will originate from the thiophene and anthracene core, making the intensity variation in this feature a good approximation of the orientation of this molecular plane. The general trend of decreasing intensity for increasing angle of incidence then qualitatively confirms the XRD results of a nearly upright anthracene core relative to the substrate. Therefore, since HB-ant-HT exhibits an intensity minimum at 60° as opposed to 75°, it must display a slightly greater tilt angle relative to the substrate normal then HB-ant-THT.

Table 5.1 shows the measured charge carrier mobility for each of these materials when fabricated into OTFT devices. These values were calculated by collaborators from the I-V characteristic of bottom gate, top contact devices fabricated under ambient conditions without additional annealing [8,40]. Interestingly, the materials with the highest and lowest mobilities of the four are those that show evidence of crystalline order, HB-ant-HT and HB-ant-THT. This suggests that the differences in mobility are due to subtle structural differences which may not be immediately apparent from the NEXAFS measurements, such as the specific degree of tilt or a cofacial versus herringbone style structure.

Table 5.1: Measured Hole mobilities calculated from I-V characteristic

	Hole Mobility (cm^2/Vs)
*B-ant-HT	0.014
†B-ant-THT	0.040
*HB-ant-HT	0.010
†HB-ant-THT	0.240

†: Ref. 8.
*: Ref. 40.

In the following sections, the nature of the stacking and electronic structure of these molecules is discussed further, with the aid of DFT calculations.

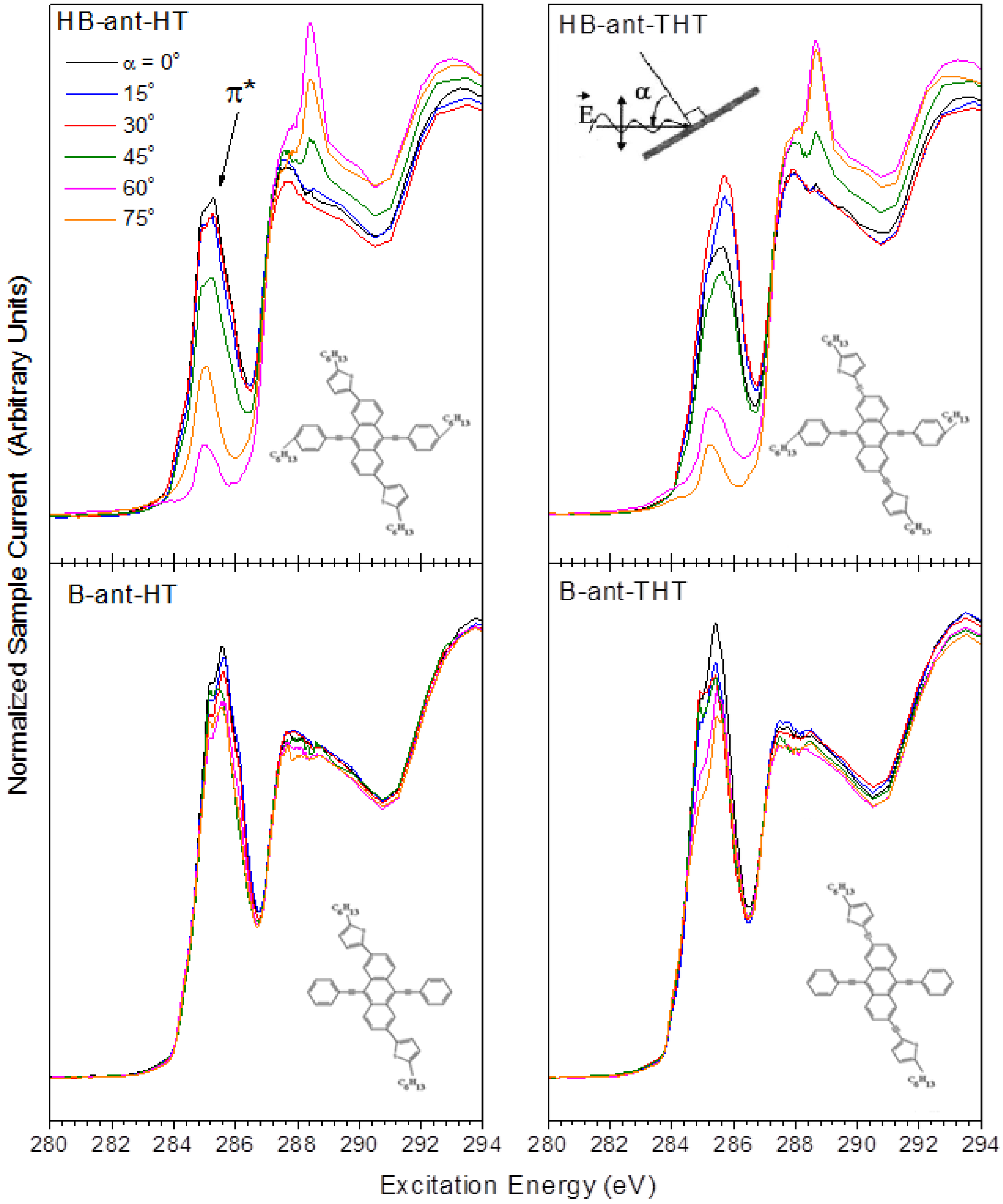

Figure 5.4. Angle resolved NEXAFS of the four anthracene-based molecules. Clear evidence of local structure is observed through polarization dependence for those molecules with additional alkyl chains.

5.1.3. DFT calculations

Shown in figures 5.5 and 5.6 are DFT simulations of the XAS measurements for HB-ant-HT and B-ant-THT. Similar calculations were performed for B-ant-HT and HB-ant-THT, but no new information was gained as the calculated spectrum from each constituent was identical to those that are already shown here. In the top panel of Fig. 5.5, NEXAFS of HB-ant-HT at normal incidence is compared to a DFT simulation and the XAS of anthracene powder. In this case, since these materials are *p*-type, the nature of the unoccupied states does not directly give insight into the charge conduction properties of these molecules. However, when comparing the spectra from all four molecules, changes in spectral features observed in the unoccupied states can indicate which molecular constituents have modified MOs due to changes in geometry.

From the top panel of Fig. 5.5, comparison with the anthracene powder immediately assigns the LUMO to have a large density on the anthracene core of the anthracene based molecules, with reduced contribution from the other molecular groups. Additionally, the sharp peak at 288.5 eV seen in the NEXAFS is shown to have a contribution from higher energy anthracene C=C π* states. The DFT calculation is a total XAS calculation containing no orientation information, and was computed as an average signal over all possible orientations. The calculated spectrum does not appear to match the lineshape of the measurement exactly, but this is a function of the broadening which is arbitrarily applied. Certainly better agreement could be obtained with more imaginative broadening, but no increased understanding would be gained from such an endeavor.

The true strength of the DFT simulations is shown in the lower panel. Here, the resonances from each constituent on the molecule are shown individually such that the

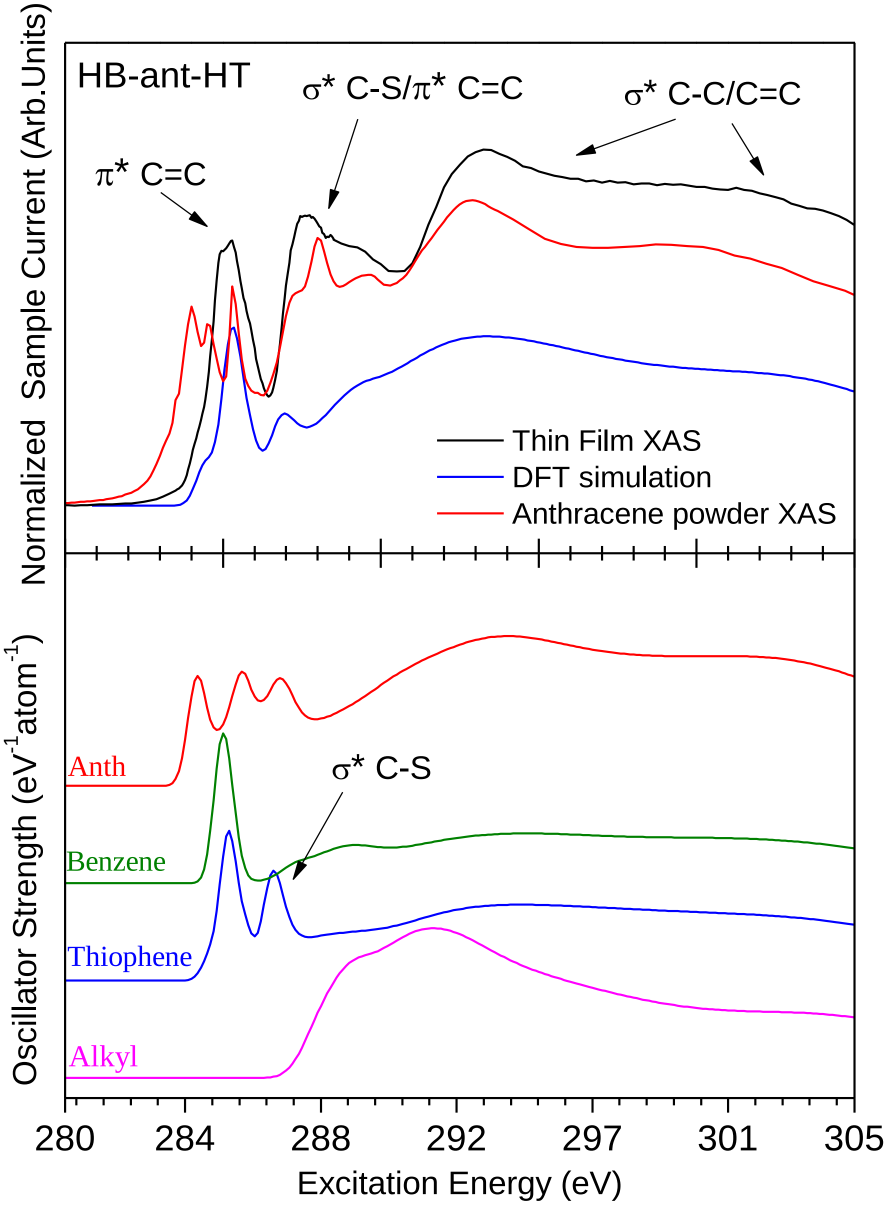

Figure 5.5. Comparison of HB-ant-HT NEXAFS to Anthracene powder and DFT XAS simulation (top panel). The bottom panel shows the contribution to calculated spectrum from each molecular constituent.

peaks in the measurement may be assigned unambiguously. The ethynyl group contribution is not shown individually, but is included with that of the benzene or thiophene when it is present. The low lying π* peak centered at 285 eV is determined from calculation to be a convolution of C 1*s* → π* (C=C) resonances from the anthracene, thiophene, and benzene groups. Also shown by calculation is a contribution from C 1*s* → σ* (C-S) excitations in the thiophene groups to the peak at 288.5 eV, commonly seen in thiophene containing materials [33]. The alkyl chains, containing no C=C bonds, do not possess any π * states and contribute only higher energy σ* orbitals above the IP which is located at ~290 eV.

Shown in Fig 5.6 is a similar analysis for B-ant-THT. Interestingly, both the anthracene and thiophene signatures are modified in this case. This material differs from HB-ant-HT in that it is lacking additional alkyl chains, and has thiophene groups with an ethynyl bridge attachment. From the DFT, we see an enhancement in the C 1*s* → σ* (C-S) resonance in the thiophene, as well as an apparent lowering in energy of anthracene LUMO states. This variation is not expected to be due to the additional alkyl chains, as they are situated relatively far away from the core, and also do not contribute any π* states. Clearly, the attachment of the thiophene has a large effect on the distribution of unoccupied states for these molecules. This suggests that they will display remarkably different bonding character, and hence take different stacking structures in thin films.

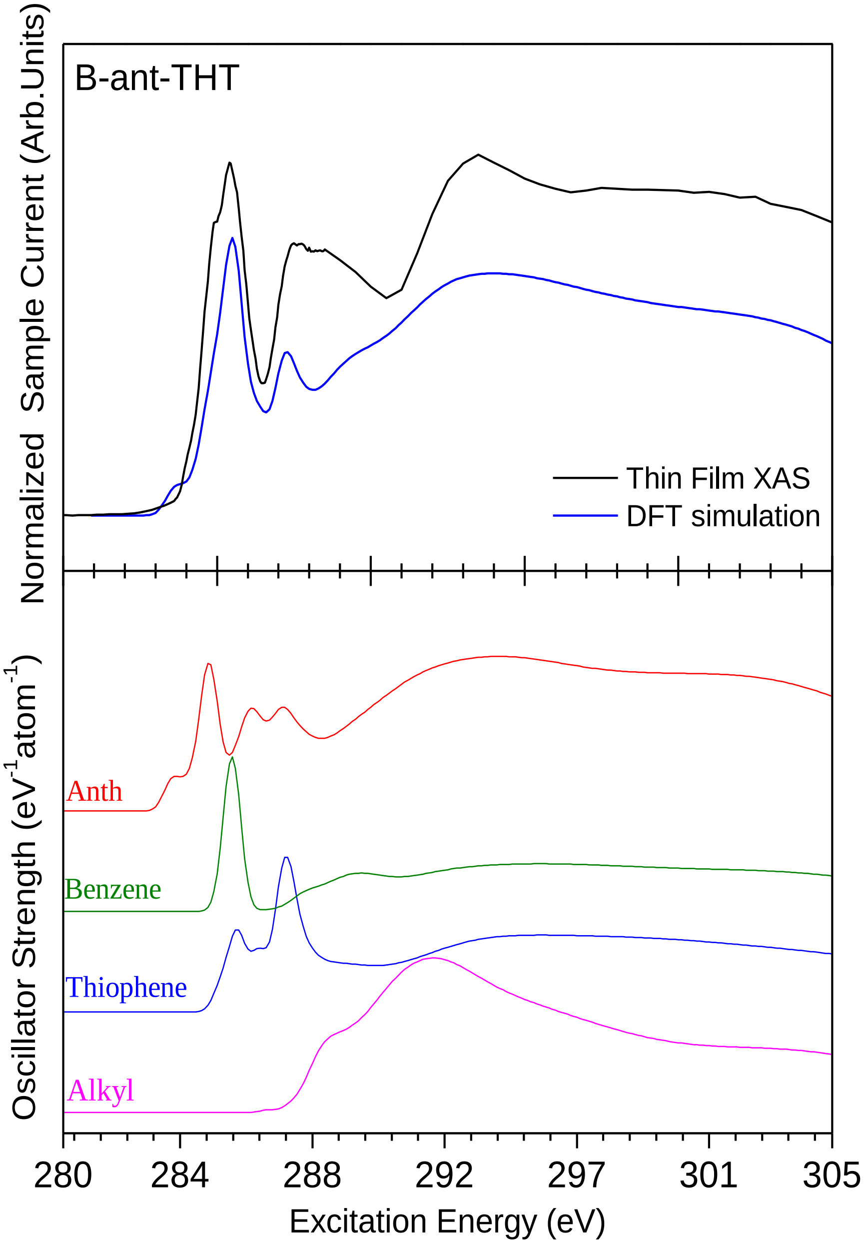

Figure 5.6. Comparison of B-ant-THT NEXAFS to DFT simulation (top panel). The bottom panel shows the contribution to calculated spectrum from each molecular constituent. Note the differences in anthracene and thiophene resonances.

5.1.4. HOMO-LUMO gap and Organic Semiconductors

The HOMO-LUMO gap describes the mean separation between these MOs in an organic material. This is roughly analogous to a bandgap in inorganic semiconductors, where the size of the gap classifies the material as an insulator, metal, or semiconductor. The HOMO-LUMO gap itself is of importance for transistor applications as it represents the amount of energy required for an electron in occupied valence states to be promoted to unoccupied conduction states. This is related to turn on voltage in transistors, which is one parameter that should be minimized as much as possible for energy efficient devices. In addition to the gap itself, the energies of the HOMO and LUMO relative to the vacuum level are also of interest as good matching between those of the semiconductor and the attached electrodes is required for efficient charge injection. However, using X-ray spectroscopy, only the energy value of the gap is obtainable through the use of second derivatives.

The use of XAS and XES to determine the HOMO-LUMO gap is not in fact a true representation of the gap in a material, as both these states involve the creation of a core hole which modifies the distribution of MOs and acts to relax outlying orbitals towards the nucleus. The true gap is that of the ground state which cannot be probed with X-ray spectroscopy, or indeed any other excited-state measurement. However, for the case of carbon, the relaxation effects are minimal as compared to a transition metal system containing occupied *d* states. In such a metal, the *p* and *d* states are highly coupled, and a core hole in *p* states will greatly modify the energy of outlying *d* states. In the case of carbon, only *s* and *p* states are present, and when a core hole is created, the 2*p* states are screened by the tightly bound 2*s* states, minimizing relaxation effects. Therefore, although XAS and XES cannot probe the true HOMO-LUMO gap, they can give a good approximation for elements without strong core hole effects.

XAS and XES are used to find the HOMO-LUMO gap by using second derivatives of the measured spectra. In molecular XAS spectra, the various unoccupied states are often well defined when taken at a high resolution beam line such as the SGM, where each peak below the IP represents a specific unoccupied bound state which may be occupied by excited electrons. Therefore, it is typically a simple matter to locate the LUMO level as the first prominent low energy peak. The location of the HOMO is by contrast often far more unclear due to the relative lack of features in C *K*α XES spectra, and often presents as a barely discernible shoulder. The use of second derivatives serves to locate these hidden shoulders since it is a representation of the curvature of a line. Once second derivatives are computed, one need only locate the first trough – which corresponds to the first peak or shoulder – in the derivative spectra as measured from the center of the gap. This is illustrated below in Fig. 5.7 for HB-ant-THT. In this case the selection of derivative features is somewhat ambiguous as the peak located at 285 eV would be the natural choice for the LUMO. However, given the previous DFT calculations which show the first anthracene resonance lower than the main resonance at 285 eV, the small shoulder at 284.25 eV is selected. This combined with the XES result yields a HOMO-LUMO gap of 2.01 eV.

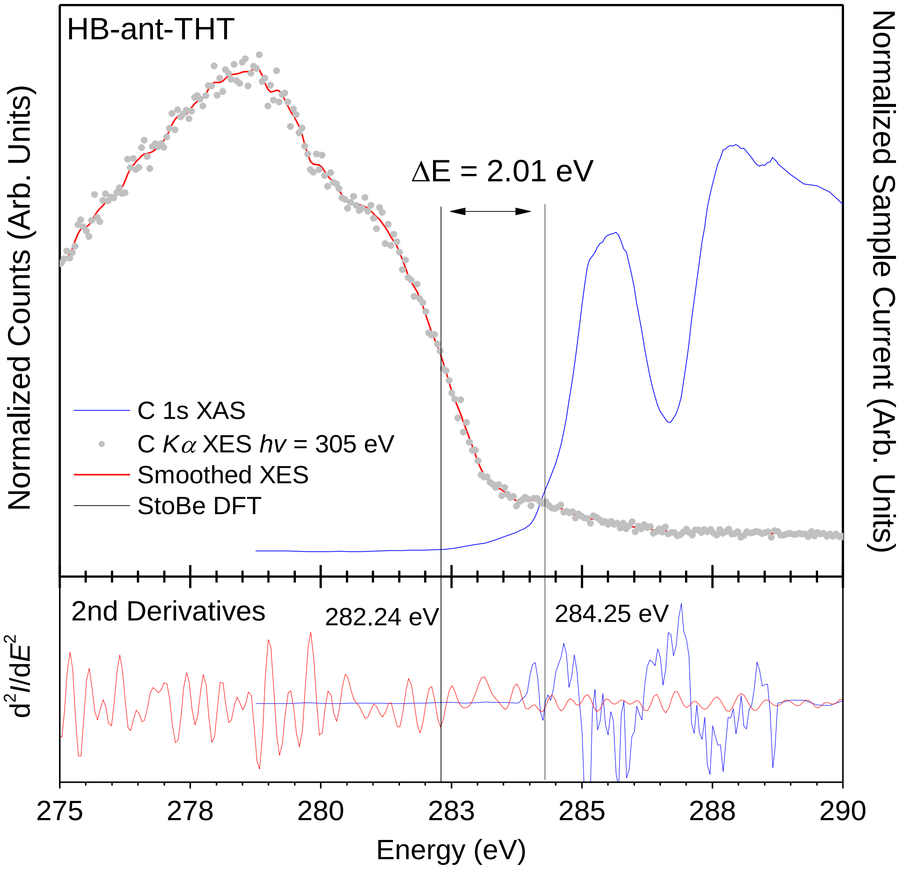

Figure 5.7. HB-ant-THT XAS and XES measurements. Second derivatives are used to find the C 1*s* →LUMO and HOMO → C 1*s* transitions, with a resulting gap of 2.01 eV.

The HOMO-LUMO gap results for the other three molecules are summarized in Table 5.2 below, and are also compared to values determined by UV-Vis spectroscopy in the literature. The values determined by XAS/XES fall within ~0.1 eV of the UV-Vis results, in good agreement. Referring to the observed energies of the HOMO and LUMO transitions, no trend is observed in the values that would correspond to the structure, and all HOMO and LUMO levels are within ~0.15 eV of each other. This indicates that the

HOMO-LUMO gap of these materials is not greatly affected by the specific structure of the films, and is more so an intrinsic property of the materials themselves.

Table 5.2: HOMO-LUMO gaps determined from XAS/XES compared to UV-Vis.

	C 1*s* →LUMO and HOMO → C 1*s* transition energies (eV)		This Work	*Ref. [8] †Ref. [40]
Material	HOMO	LUMO	Thin Film (eV)	UV-Vis E_g^{opt} (eV)
B-ant-HT	282.10	284.37	2.27	†2.19[a], 2.21[b]
B-ant-THT	281.85	284.00	2.15	*2.20[a], 2.16[b]
HB-ant-HT	281.85	284.05	2.20	†2.17[a], 2.15[b]
HB-ant-THT	282.24	284.25	2.01	*2.15[a], 2.14[b]

[a]: before annealing
[b]: after annealing

5.1.5. C *Kα* XES and the HOMO

As stated previously, the four anthracene molecules are *p*-type semiconductors, meaning that the most efficient charge conduction occurs through hole transfer. A hole is generated when an electron in the HOMO is excited to unoccupied LUMO states. Once separated, both the electron and hole may migrate through the material, subject to the specific environment of the MOs that they now occupy. In the case of *p*-type materials, holes are transmitted much more easily, which is primarily due to a favorable distribution of HOMO states as opposed to LUMO. In order to probe the occupied hole conduction states, XES measurements were performed for these materials at Beamline 8.0.1, which are summarized in Fig. 5.7. Unfortunately, the spectra show very little structure, with

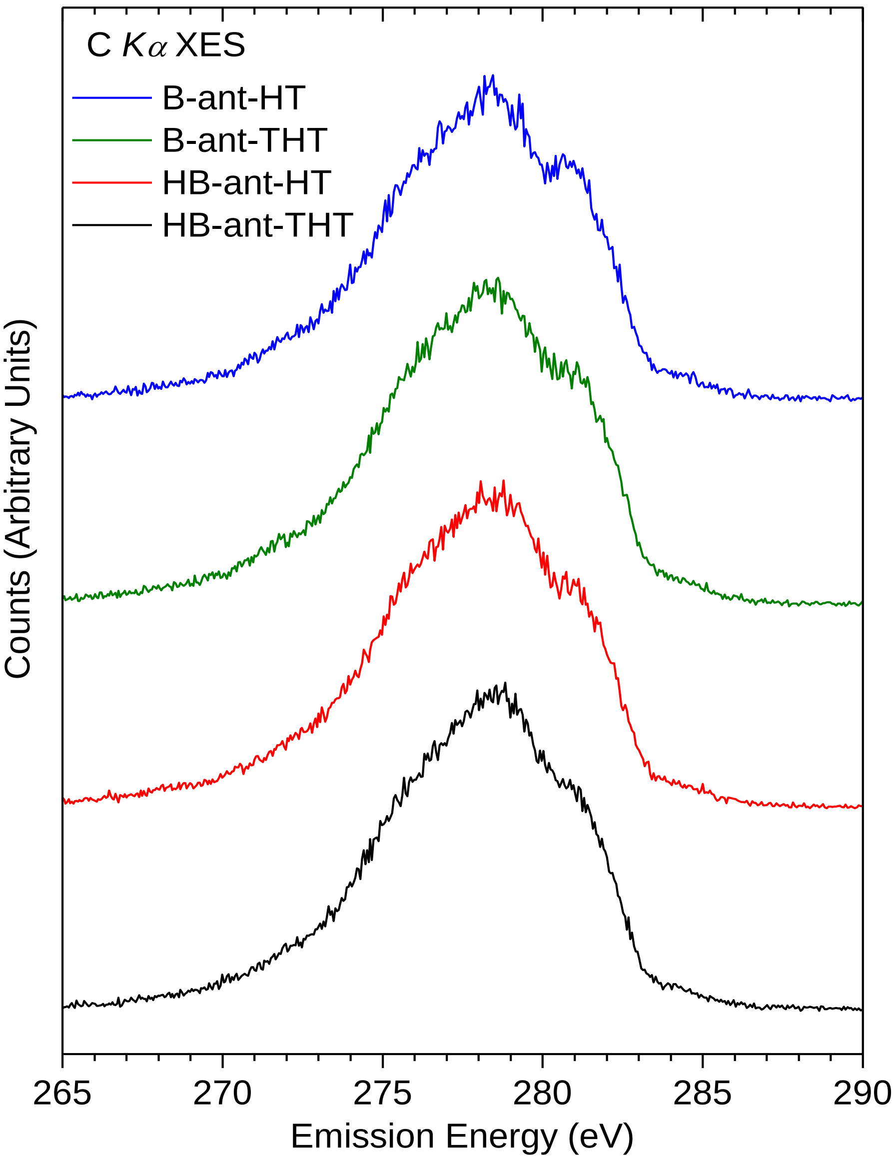

Figure 5.8. XES measurements of the anthracene based materials. Few spectral features are evident, with all measurements appearing very similar.

only one high energy shoulder clearly visible. From these measurements there is also no clear change in the HOMO level, and only a minor energy shift was discernible through the use of second derivatives. A lack of features is common for organic materials where the occupied C states tend to be very energy degenerate, preventing the appearance of any meaningful structure. From the DFT calculations shown previously, it was clear from which parts of the molecule each unoccupied resonance arose from, and a similar analysis is performed here using Gaussian03 for occupied states, shown in Fig 5.9.

This figure presents calculated HOMO isosurfaces for all four molecules. The isosurfaces show the distribution of MOs across each of the molecules, and are a useful presentation tool for identifying the physical location of certain MOs. From the results, there is very little change between the molecules, with the HOMO in each case relegated to the anthracene, thiophene, and ethynyl groups, with only a small contribution from the benzene. This result was not unexpected given the structural similarities between the molecules, and implies that observed differences in electrical performance between these molecules are the result of differing thin film structure as opposed to a variation in molecule electronic structure. From comparison with the values shown in Table 5.1, the additional HOMO conjugation provided by the ethynyl groups appears to increase the mobility by increasing the area of possible HOMO overlap between neighbouring molecules, providing additional conduction pathways. However, these factors are not sufficient to explain the order of magnitude increase in mobility for HB-ant-THT, further suggesting that a variation in molecular stacking structure is the root of differing charge transport properties.

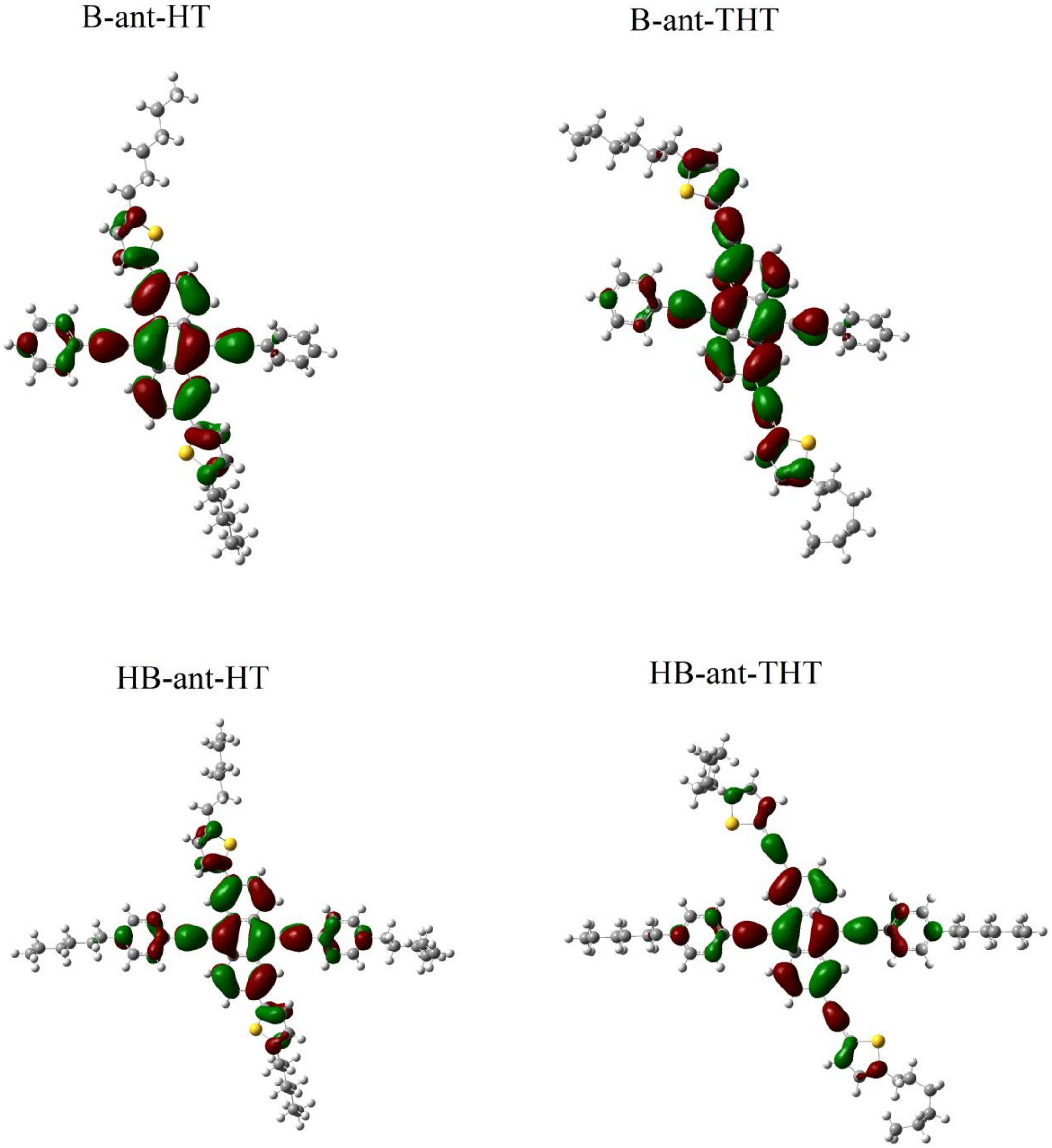

Figure 5.9. HOMO isosurfaces. This MO is extremely similar between all four molecules, and is located primarily on the anthracene, thiophene, and ethynyl groups.

.

5.1.6. Molecular orientation

In principle, the polarization dependence on π* features in NEXFS spectra can be used to quantitatively determine the tilt angle of the π* vector for a given resonance relative to the substrate, and therefore determine the local orientation of the molecules. Such an analysis was first described by Stöhr and Outka [35], and has been used to great effect in finding molecular orientation of organic materials such as P3HT and pentacene [33]. However, in this case, the only prominent features appear as a convolution of excitations from all parts of the molecule. In order to successfully quantify the orientation of each constituent, the resonances need to be separated and the intensity change of each analyzed individually. In this case however, this is not possible, and such an analysis cannot be performed.

From the polarization dependence, it is still possible to estimate the orientation. As stated previously, NEXAFS indicates a nearly upright structure for HB-ant-HT and HB-ant-THT, with a slightly greater tilt angle indicated for HB-ant-HT. From comparison with the other two materials, it is clearly the additional alkyl chains which induce the structural ordering. The tilt variation is then the result of the ethynyl bridge thiophene attachment between these materials, but as mentioned previously this slight difference is not sufficient to explain the order of magnitude difference in charge carrier mobility. To explain this, such a large disparity in mobility must be due to a similar large variation in structure that is not detectable with XRD or NEXAFS. In the case of HB-ant-THT, the structure may be a variation of a cofacial π-stack, such as slipped stack (Fig. 5.3), which allows for favourable HOMO overlap between neighbouring molecules and the observed high mobility. The difference in thiophene attachment for HB-ant-HT is then predicted to not only increase the tilt, but also precipitate a herringbone structure. This configuration would present very similar XRD and NEXAFS results as a cofacial structure, as these techniques probe the lattice spacing and molecular tilt, but not intrinsically the rotation of the molecules relative to each other. Such a herringbone structure would explain the much lower mobility of HB-ant-HT because in this configuration the HOMO of one molecule would overlap with only the alkyl chain MOs of a neighbouring molecule. The length of the chains will then simply separate the molecules to such an extent that favourable HOMO coupling could not possibly occur. Although orbital overlap does not always guarantee increased mobility, materials that do not present it very rarely display good performance. In those rare cases, the material is made of small molecules such as pentacene, without large endgroups such as the alkyl chains in this case, and therefore favorable overlap can still occur in a herringbone structure.

5.1.7. Conclusions

NEXAFS of these materials clearly shows the presence of local structure for two of the four, with a polarization dependence indicating that the molecules are stacked nearly upright with a slight tilt, in agreement with XRD results. The electronic structure of both occupied and unoccupied states has been further analyzed using the combination of NEXAFS, XES and DFT calculations. It is clear that molecules with an anthracene core and thiophene functional groups provide a well conjugated HOMO which is ideal for *p*-type conduction. The efficiency of transfer between neighbouring molecules is then nearly entirely dependent on the molecular stacking. The addition of alkyl chains has been shown to produce an ordered structure, but the nature of the stacking, be it herringbone or cofacial, is also influenced by the nature of the other functional groups.

In this case, the ethynyl attachment of the thiophene is concluded to result in a large variation in stacking, in correlation with mobility measurements. Knowledge that a slight variation in thiophene attachment can have such a large effect on film stacking structure is of great importance for fabrication of new materials. In particular, work may be continued with structures related to these to potentially produce a whole family of acene-based materials with ordered structure achieved without the need for annealing.

5.2. PCBM

Among the currently commercially available organic semiconductor materials, the fullerene (C_{60}) and its derivatives are some of the most common and efficient *n*-type organic semiconductors. In particular, PCBM has been shown to have high solubility in common solvents [50]. It is actively used in fabrication of OPVs as an electron acceptor and OTFTs, usually in the form of films blended with *p*-type conjugated polymers such as P3HT [51-54].

The control of film crystallinity and knowledge of electronic structure have been shown to be a requirement for improved device performance, particularly for blended devices [54,55]. In the case of PCBM, crystallization depends strongly on the deposition process used. When PCBM is deposited on Au(111) with film thicknesses of a few monolayers, a well ordered structure of PCBM dimers is formed that is governed by hydrogen bonding between side chains and the substrate surface [56,57]. With greater coverage, however, the high order is reduced and a nearly amorphous structure results with unknown side chain effects. Bulk crystal structure calculations of PCBM have been performed [58], and indicate that the side chain may act to produce several possible homogeneous structures, each with different electronic properties and morphologies. Films fabricated by spin coating, as reported by Yang *et al*. [59], indicate such bulk homogeneity with varying morphologies depending on the deposition parameters. From these results, side chain and substrate bonding appear to almost completely determine crystal structure in monolayers, but it is not clear what effect the side chain has on bulk structure beyond inducing homogeneity. In addition to influence on crystallization, the side chain has been shown to modify PCBM's electronic properties [58,60-62]. Akaike *et al*. [61] reported a lifting of the degeneracy of the LUMO of C_{60}, which has also been found for C_{60} functionalized with 11-amino-1-undecane thiol (11-AUT) self-assembled monolayer [62]. The side chain is also reported to contribute to higher energy MOs, and is thought not to be directly involved in conduction [58,60,61].

The study undertaken here analyzes the effects of the side chain on both crystal and electronic structure of PCBM using a combination of C 1*s* NEXAFS, C *K*α XES, and DFT calculations. The analysis and results are presented in the following sections.

5.2.2. NEXAFS Measurements

Fig. 5.10 presents angle-resolved C 1*s* NEXAFS measurements of the PCBM spin coated film measured in TFY mode. These measurements probe the bulk structure of the buried PCBM layer without surface contribution due to the gold capping layer. The spectra show a decrease in absorption intensity with increasing incident angle measured from normal to the substrate for the first three lowest energy π* peaks (284.5 eV, 285.8 eV, 286.3 eV). The pronounced angular dependence of the intensity of C_{60}-derived π* peaks is unexpected due to the high symmetry of this structure. This polarization dependence observed in C_{60}-derived π^* absorption peaks indicates that the side chain reduces the high symmetry of the C_{60} π^* network from icosahedral (I_h) to C_1. Specifically, the LUMO is no longer evenly distributed and now possesses a π^* vector that points radially outward from the C_{60} asymmetrically. This has been observed experimentally for other functionalized fullerenes [62], but is not indicated by orbital density calculations [60,61]. The reduced orbital symmetry further allows for determination of crystal structure, with the pattern of polarization dependence in the π^* excitations indicating a MO vector that points preferentially parallel to the substrate plane.

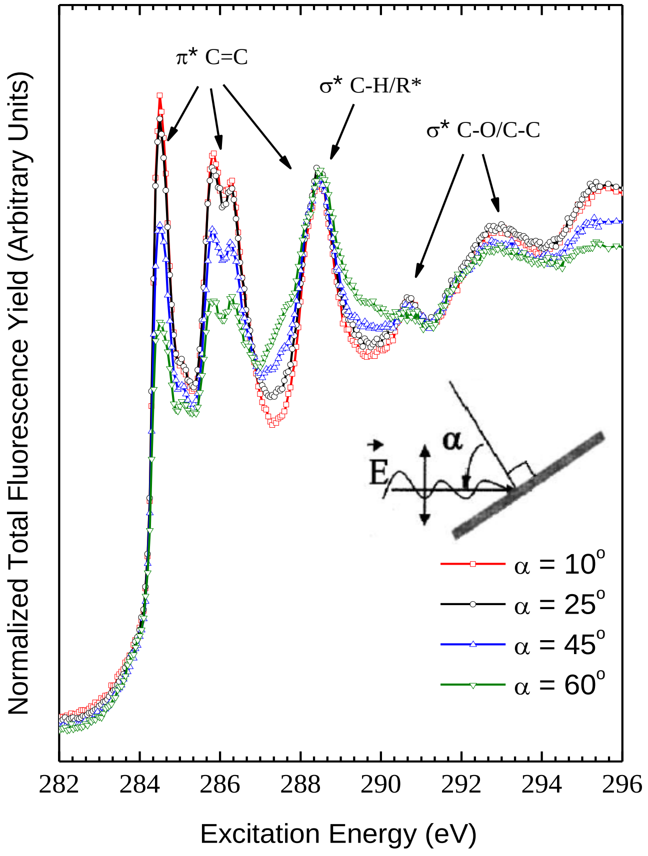

Figure 5.10. Angle-resolved C 1*s* XAS measurements of PCBM thin film measured in TFY mode. α represents the angle of incidence of X-ray radiation measured from the substrate normal.

Fig. 5.11 shows by calculation a phenyl contribution to the 285.8 eV π* peak which is discussed below, and this is further verified by the pattern of intensity loss NEXAFS measurements, tabulated in Table 5.3.

Table 5.3. Tabulated peak intensities for PCBM Angle Resolved NEXAFS

Peak Energy (eV)	284.5	285.8	286.3
Incident Angle α (°)	Normalized Absorption Intensity (arb. units)*		
10	1.054	0.954	0.907
25	1.120	0.931	0.896
45	0.836	0.829	0.803
60	0.676	0.708	0.718

*Intensities are recorded from spectra normalized to a uniform background at 315 eV.

At near normal incidence the 285.8 eV peak shows greater intensity then the nearby 286.3 eV peak. At 60° incidence it has decreased to a lower intensity than its neighbor, and the double peak begins to resemble that of the C_{60} powder. The spectral change is due to a contribution from π-orbitals projecting perpendicular to the plane of the ring with a reduced cross section for grazing incidence indicating the plane of the ring is preferentially perpendicular to the substrate plane. Similarly, the broad σ* resonance above the IP (not shown) shows an angular dependence consistent with σ -bonds along the length of the polyethylene chain oriented preferentially parallel to the plane of the substrate. The change in σ* resonance is not considered to originate from the C_{60} because these excitations arise from C-C bonds which should show no variation due to symmetry. Although orientation information may be obtained from the measurements about the C_{60} π* MOs, the exact orbital configuration is unclear. Given that the orbitals around the attachment point are shifted in energy, it is reasonable that the remaining π* MOs are distributed across the rest of the C_{60} surface and point radially outward. In this configuration, the highest density of coplanar MO vectors is a ring around the center of the C_{60}.

5.2.3. DFT calculations

Fig. 5.11 presents the C 1*s* NEXAFS spectra of a PCBM thin film and C_{60} powder reference compared to the simulated PCBM spectrum (a) and the calculated spectral contributions to absorption features from C_{60} backbone and side chain (b). Comparison of the PCBM and C_{60} NEXAFS spectra assigns most of the resonance intensities of peaks at 284.5 eV (LUMO), 285.8 eV, 286.3 eV, and 288.4 eV, as contributions from the C_{60} backbone. This result is expected because due to its comparative size, the C_{60} must provide most of the unoccupied states in PCBM. Given that the C 1*s* IP of C_{60} is located at approximately 289.6 eV [63], the first four low energy peaks represent π* resonances and those above the IP constitute σ* resonances [36,64,65]. The simulations shown in Fig. 5.11(b) can be used to assign the absorption peaks as originating from specific excitations within the molecule (see labels on Fig. 5.10).

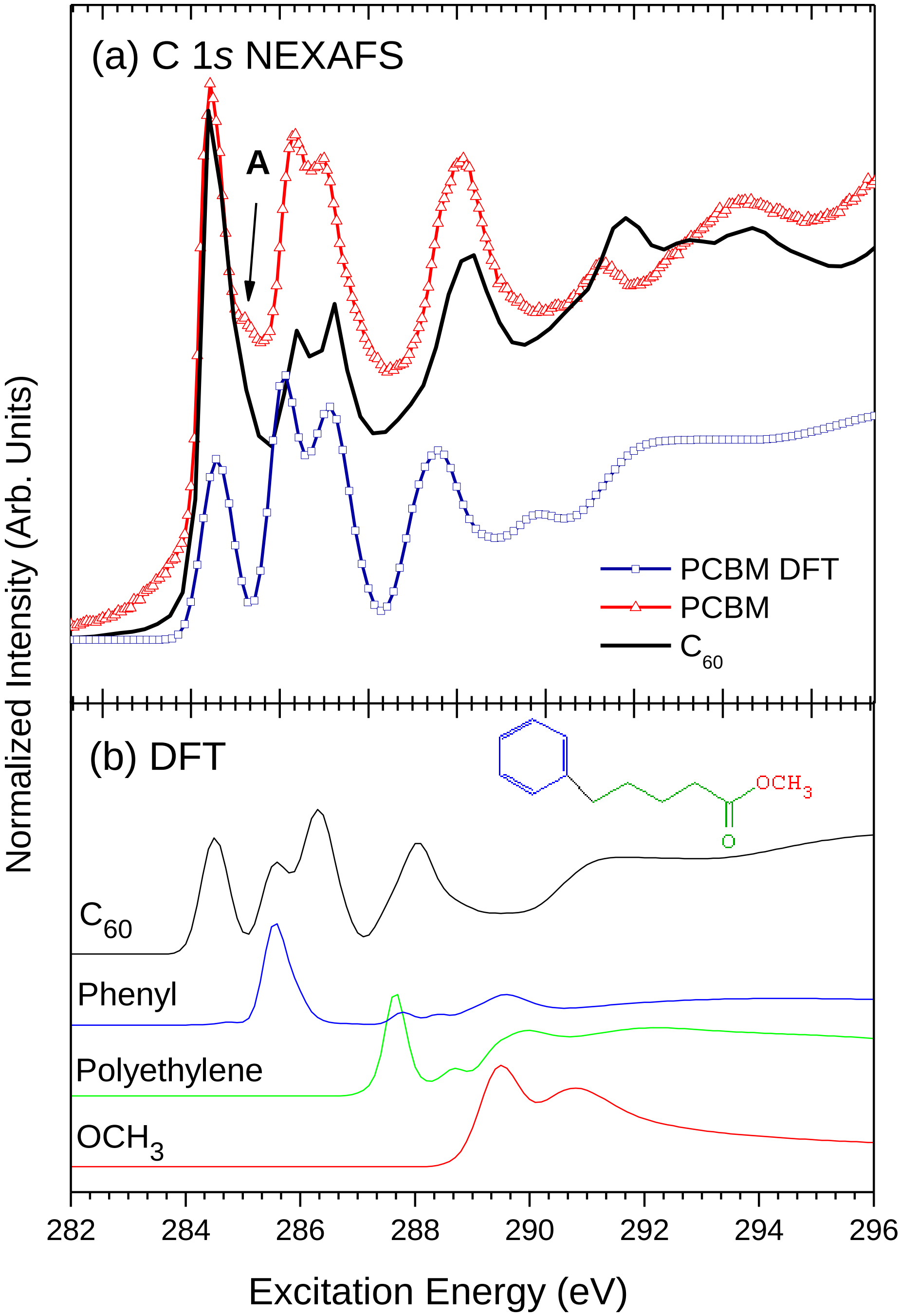

Figure 5.11. (a) Comparison of C 1*s* XAS spectra of PCBM spin-coated film measured in TFY mode with simulated PCBM spectrum and the measured reference spectrum of C_{60} powder and (b) the calculated XAS spectra for individual groups within PCBM molecule and the inset shows the molecular groups coloured to match the corresponding line colour of simulated spectra.

The π* resonances at 284.5 eV, 285.8 eV and 286.3 eV arise from C 1*s* → π* (C=C) excitations [54,63], in the C_{60}, but also with a contribution from the aromatic phenyl ring in the first of the double peaks at 285.8 eV, shown by calculation. This is consistent with the measurements as it accounts for the notably larger intensity of the first peak in the PCBM measurement when compared to the C_{60}. It has been shown by Kondo *et. al*. [64] for C_{60} films that this peak represents a highly dispersive MO which contributes to intermolecular interaction in the bulk phase. This suggests that the phenyl ring may influence bulk intermolecular interaction by providing additional dispersed MOs. The peak at 288.4 eV is as a combination of C 1*s* → π* (C=C) excitations in the C_{60} and transitions to σ* (C-H) and molecular Rydberg orbitals (R*) arising from the polyethylene chain [36,55,66]. The higher energy σ* peaks are a combination of C 1*s* → σ* (C-C) transitions from all parts of the molecule [54,66]. The new feature not present for C_{60} is the after-edge shoulder occurring at 285.1 eV (labeled A). This is associated with the C atoms around the side chain attachment point. The attachment of the side chain breaks I_h orbital symmetry of the C_{60}, causing a shift in MO energy near the attachment point [61,62]. A shift to higher excitation energy corresponds to a shift to lower ionization energy, which indicates a donation of electrons from the side chain to the C_{60} near the attachment. This is also manifested in a slight shift of the PCBM unoccupied states (0.05 eV) to higher energy.

5.2.4. Thin Film Stacking Structure

Given the above orientation information derived from NEXAFS, the possible bulk stacking structure motifs may be determined for this PCBM film. Additional calculations were also performed using the GAUSSIAN03 to determine if the attached side chain introduces a molecular dipole to the C_{60} structure due to its asymmetry. To determine this, a DFT total energy calculation using a previously optimized structure was performed. It was found that the side chain induces a dipole moment which points along the length of the polyethylene chain with a magnitude of 3.83 D. This will have the effect of aligning the molecules in such an arrangement that accommodates the dipole. In the absence of a substrate to influence orientation, the induced dipole will act with Van der Waals forces to self-organize the bulk structure. Given the orientation of the molecular constituents and the presence of a dipole, there are several crystal structures that agree with the measurements. Fig. 5.12 (a) places the molecules all oriented the same direction, in agreement with the NEXAFS results and molecular dipole. Structures (b) and (c) are produced by rotations about the horizontal axis (polyethylene chain) of the upper left and bottom right molecules by 180° in (b) and 90° in (c). Fig. 5.12 (d) is produced by a 180° rotation about the vertical axis (plane of the phenyl ring) of the two left side molecules. These four structures allow for formation of hydrogen bonds between side chains which have been shown to highly influence PCBM structure on surfaces [56,57]. In particular, structure (d) supports stronger hydrogen bonding between functional chains. This type of bonding will compete with the effect of the dipole to ultimately determine bulk structure. Furthermore, since the exact distribution of π * states on the C_{60} is unclear, any structure similar to those in Fig. 5.12 where the molecules are allowed to rotate around a reference axis running along the length of the polyethylene and through

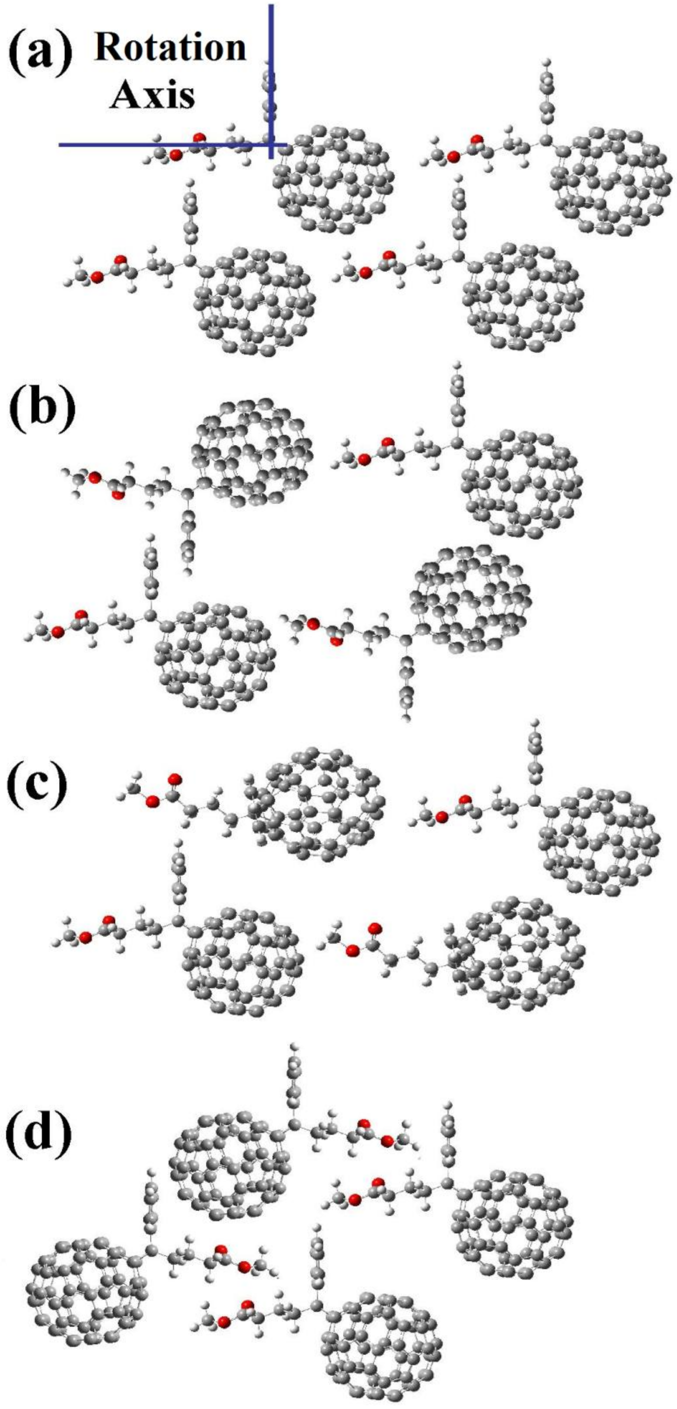

Figure 5.12. Four possible stacking structures that are supported by the angular dependence seen in the NEXAFS measurements. (d) shows an arrangement which allows for stronger hydrogen bonding between functional chains

the plane of the phenyl is supported by the measurements (blue rotation axis, Fig. 5.12 (a)). The true bulk material is therefore a combination of such allowed structures.

5.2.5. HOMO-LUMO Gap

NEXAFS and XES probe the unoccupied and occupied MO states, respectively, and so the band-gap energy of PCBM may be determined by superposing C *K*-edge NEXAFS and XES spectra. Fig. 5.13 shows non-resonant C *K*α XES and C 1*s* NEXAFS measurements for powder PCBM. In the lower panel, the second derivatives of NEXAFS and XES spectra were used to place the HOMO at 282.63 eV and the LUMO at 284.50 eV with a resulting energy gap of 1.87 eV for powder PCBM. This is in agreement with recently reported values of 1.8 – 1.9 eV [67,68]. In this case, the second derivative of the XES spectrum is performed on a fitted line for clarity with the same result obtained otherwise.

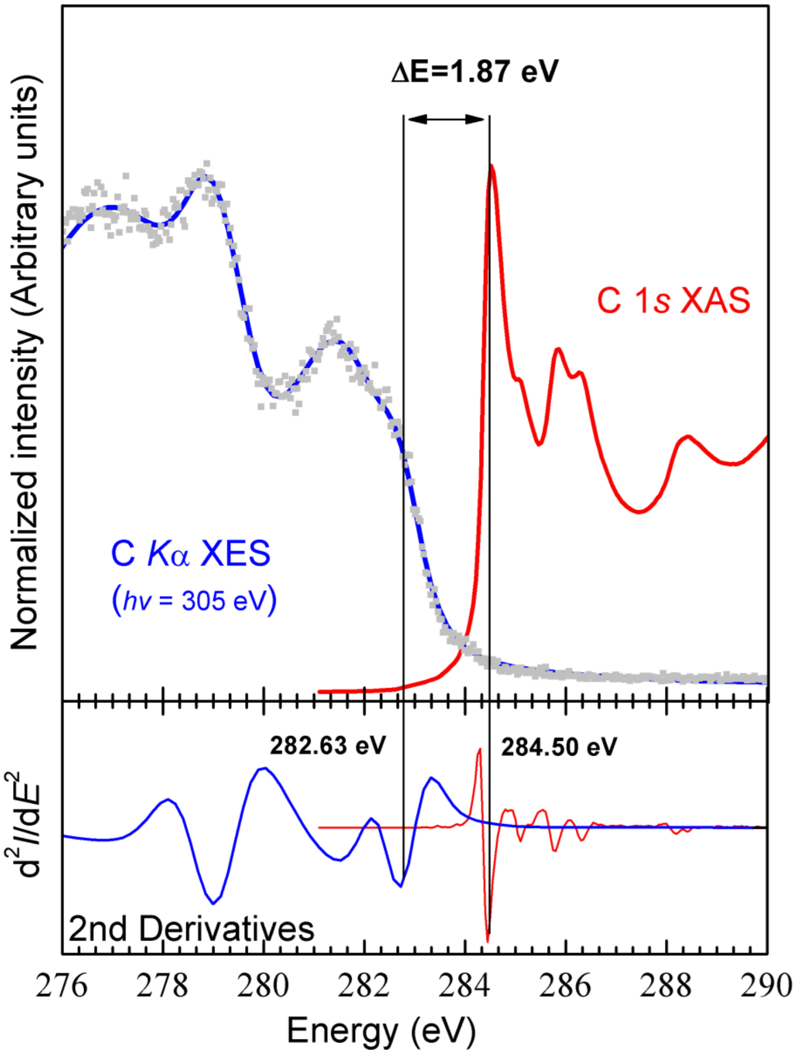

Figure 5.13. PCBM XES and XAS powder spectra, with smoothing applied to the XES. Second derivatives of the smoothed XES and measured XAS spectra are used to determine the energies of the HOMO and LUMO, and a resulting gap of 1.87 eV.

5.2.6. Conclusions

The PCBM side chain has been shown to influence both MO distribution and bulk crystal structure. NEXAFS clearly shows the presence of a partially lifted LUMO degeneracy around the attachment point. Pronounced angular dependence of π* features known to originate from the C_{60} suggests an asymmetrical MO distribution and is clear evidence of crystalline structure. NEXAFS polarization dependence has also been observed for C_{60} functionalized with 11-AUT [62], where the presence of the SAM is expected to induce order. In the case of PCBM, the side chain behaves similar to 11-AUT to influence order by way of hydrogen bonding and molecular dipole moment. With the LUMO of PCBM arising exclusively from its C_{60} character, n-type conduction will occur most readily between C_{60} backbones where MOs overlap. Since the C_{60} LUMO MOs are predicted to have a ring like distribution around the center of the structure, an ordered crystal structure that allows for such overlap is required for efficient conduction. The correlation between these results and those in the literature shows that any functionalized C_{60} derivative should display a similar asymmetrical MO distribution, as well as structure influenced by the nature of the functionalizing group. This fact should be taken into account when optimizing the crystal structure of thin films containing C_{60} derivatives for best performance.

6. Summary and Future Research

The following section provides a summary of the material properties determined for the systems reported here, as well as other systems currently under study and directions for future research. The main focus of future studies is the expansion of research interests from the pure study of material properties, to the application of those studies in actual device fabrication. To that end, new equipment has recently become available that includes a physical vapor deposition (PVD) system and a solar simulator.

6.1. Properties of Materials Studied

NEXAFS measurements were used to probe the local molecular structure of the four anthracene based materials, identifying two of them as possessing an ordered structure. From the polarization dependence, it is determined that these molecules have a nearly upright orientation, with the plane of the anthracene core oriented nearly normal to the substrate with a slight tilt. The electronic structure of both occupied and unoccupied states was further examined, with very little variation observed between the molecules concerning energy locations of the HOMO and LUMO. Using DFT calculations, XAS simulations were performed which identify origin of π^* resonances, showing that both the HOMO and LUMO are located primarily on the anthracene, thiophene, and ethynyl groups. These findings are correlated to mobility values collected from OTFT devices of these materials, and due to the absence of electronic structure differences, the mobility variation is concluded to be a result of differing film structure. Specifically, HB-ant-THT exhibits a variation of cofacial stacking, where HB-ant-HT is herringbone which accounts for its much lower charge carrier mobility.

The solar cell material PCBM was examined with spectroscopy techniques to probe the effects of the functional chain on electronic and stacking structure. Angle resolved NEXAFS in TFY mode was used to probe the bulk of a thin film, showing a polarization dependence in the LUMO states. This indicates that the functional groups modify the distribution of LUMO states on the C_{60} backbone, removing its high symmetry. The polarization dependence was further used with the help of DFT simulations to project the possible stacking structures that bulk PCBM takes in spin coated films. This information is applicable to other functionalized fullerenes as well, and will help in the understanding of carrier transport in blended thin films.

6.2. Future small molecule systems

For the purpose of device fabrication, many different organic materials can be considered to be good candidates for new devices. Presently, the anthracene-based molecules are under study, and following a publication regarding them, larger samples of them will be acquired from collaborators and used to fabricate OTFTs. Although the I-V characteristic has already been studied, the optimized recipe for a high performance device has not yet been determined.

New systems that were not discussed here but are currently under study include pentacene and two derivatives, its n-type counterpart perfluoropentacene (PFP), and a soluble variety, 6,13-bis(Triisopropylsilylethynyl) (TIPS) Pentacene. Pentacene and PFP are not soluble, and thin film samples were originally acquired from collaborators. These molecules are candidates for solar cell devices, and blended samples deposited on different substrates are of interest to study the thin film structure and morphology. For this both X-ray spectroscopy techniques as well as XRD will be used to study the stacking and electronic structure. Surface science techniques such as AFM and scanning tunneling microscopy (STM) will also be used to examine the morphology and probe the surface DOS.

TIPS-pentacene is a soluble pentacene derivative that was created to allow spin coating of this high mobility material for OTFTs [47]. Currently an XRD study is underway on this material to study the effect of different substrates and solvents on thin film structure, headed by Jay Forrest, a graduate student at the University of Saskatchewan. One future study on this material would be to exfoliate a thin film from a substrate, and measure the buried interface. This would give insight into the ~50 nm of film next to the dielectric where charge conduction occurs in transistors.

Several other systems are under study for the use in thin film transistors and solar cells, including PDIF-CN2 and two other related materials that are high mobility *n*-type organic semiconductors. For solar cells, blends of materials such as PC[70]BM, a version of PCBM based on a C_{70} molecules, and Poly(2-methoxy-5-(3’-7’-dimethyloctyloxy)-1,4-phenylenevinylene) (MDMO-PPV). Insight into the characteristics of these materials will aid in the optimization of thin film recipes and the development of new device architectures.

6.3. Physical Vapor Deposition and Solar Simulation

In order to fabricate solar cell and transistor devices out of diverse materials, fabrications methods beyond spin coating are required. Physical vapor deposition is a technique which can be used to deposit thin layers of most materials onto any substrate. This is accomplished by direct heating of a crucible under high vacuum by specially designed furnaces capable of reaching temperatures in excess of 2000 ºC, with the desired material within. Once hot enough, the material will be vaporized, and deposited on a rotating substrate stage directly above it. This or a similar vaporization method is required for the deposition of metals, such as for electrodes, which are not soluble and cannot be spin coated. In the coming year, this equipment will be commissioned for use, and ultimately used to fabricate transistors and solar cell devices. Plans are also in place to add a vacuum transfer arm and glove box, and possibly a vacuum sample stage, so that air sensitive materials may be used in fabrication and measured under vacuum.

In addition to expanding fabrication equipment, characterization equipment for both solar cells and transistors has been purchased. A solar simulator is a device used to simulate the light spectrum that comes from the sun. In order to measure the power conversion efficiency of solar cells, they are illuminated with the solar simulator, while simultaneously measuring their I-V characteristic. The I-V measurement is accomplished with a sample stage equipped with probes attached to a source meter, and is appropriate for both solar cells and transistors. With this new equipment, a variety of new materials may be used to fabricate and test actual devices.

7. References

1. Q. Meng, H. Dong, W. Hu, D. Zhu. *J. Mater. Chem.* DOI: 10.1039/c1jm10243e (2011).

2. H. Yan , Z. H. Chen , Y. Zheng , C. Newman , J. R. Quinn , F. Dotz , M. Kastler , A. Facchetti. *Nature.* **457**, 679 (2009).

3. M. Marinkovic, E. Hashem, K.-Y. Chan, A. Gordjin, H. Stiebig, D. Knipp. *App. Phys. Lett*, **97**, 073502 (2010).

4. C.-W. Chen, T.-C. Chang, P.-T. Liu, H.-Y. Lu, K.-C. Wang, C.-S. Huang, C.-C. Ling, T.-Y. Tseng. *IEEE Electron Device Lett*. **26**, 731 (2005).

5. M. A. McCarthy, B. Liu, E. P. Donoghue, I. Kravchenko, D. Y. Kim, F. So, A. G. Rinzler. *Science*. **332**, 570 (2011).

6. A. C. Arias, J. D. Mackenzie, I. McCulloch, J. Rivnay, A. Salleo. *Chem. Rev*. **110**,
3 (2010).

7. C. D. Dimitrakopoulos, P. R. L. Malenfant, *Adv. Mater*. **14**, 99 (2002).

8. K. H. Jung, S. Y. Bae, K. H. Kim, M. J. Cho, K. Lee, Z. H. Kim, D. H. Choi, D. H. Lee, D. S. Chung, C. E. Park. *Chem. Comm*. 5290 (2009).

9. P. Hohenberg, W. Kohn. *Phys. Rev.* **136**, 864 (1964).

10. W. Kohn, L. J. Sham. *Phys. Rev*. **140**, 1133 (1965).

11. K. Hermann, L.G.M. Pettersson, M.E. Casida, C. Daul, A. Goursot, A. Koester, E. Proynov, A. St-Amant, D.R. Salahub, Contributing authors: V. Carravetta, H. Duarte, C. Friedrich, N. Godbout, J. Guan, C. Jamorski, M. Leboeuf, M. Leetmaa, M. Nyberg, S. Patchkovskii, L. Pedocchi, F. Sim, L. Triguero, A. Vela, *StoBe-deMon version 3.0*, (2009).

12. M. J. Frisch, G. W. Trucks, H. B. Schlegel, G. E. Scuseria, M. A. Robb, J. R. Cheeseman, J. A. Montgomery, Jr., T. Vreven, K. N. Kudin, J. C. Burant, J. M. Millam, S. S. Iyengar, J. Tomasi, V. Barone, B. Mennucci, M. Cossi, G. Scalmani, N. Rega, G. A. Petersson, H. Nakatsuji, M. Hada, M. Ehara, K. Toyota, R. Fukuda, J. Hasegawa, M. Ishida, T. Nakajima, Y. Honda, O. Kitao, H. Nakai,

M. Klene, X. Li, J. E. Knox, H. P.Hratchian, J. B. Cross, V. Bakken, C. Adamo, J. Jaramillo, R. Gomperts, R. E. Stratmann, O. Yazyev, A. J. Austin, R. Cammi, C. Pomelli, J. W. Ochterski, P. Y. Ayala, K. Morokuma, G. A. Voth, P. Salvador, J. J. Dannenberg, V. G. Zakrzewski, S. Dapprich, A. D. Daniels, M. C. Strain, O. Farkas, D. K. Malick, A. D. Rabuck, K. Raghavachari, J. B. Foresman, J. V. Ortiz, Q. Cui, A. G. Baboul, S. Clifford, J. Cioslowski, B. B. Stefanov, G. Liu, A. Liashenko, P. Piskorz, I. Komaromi, R. L. Martin, D. J. Fox, T. Keith, M. A. Al-Laham, C. Y. Peng, A. Nanayakkara, M. Challacombe, P. M. W. Gill, B. Johnson, W. Chen, M. W. Wong, C. Gonzalez, and J. A. Pople, *Gaussian 03, Revision E.01*, Gaussian, Inc., Wallingford CT (2004).

13. J.C. Slater, K.H. Johnson*, Phys. Rev. B.* **5**, 844 (1972).

14. S. Huzinaga, J. Andzelm, M. Klobukowski, E. Radzio-Andzelm, Y. Sakai, H.Tatewaki, *Gaussian Basis Sets for Molecular Calculations*. Elsevier: Amsterdam (1984).

15. K. Hermann, L. G. M. Pettersson. *Documentation for StoBe2011*. (Version 3.1) (2011)

16. J. P. Perdew, K. Burke, M. Ernzerhof. *Phys. Rev. Lett*. **77**, 3865 (1996).

17. A. Becke. *Phys. Rev. A.* **38**, 3098 (1988).

18. http://www.fhi-berlin.mpg.de/KHsoftware/StoBe/XAS2.html. *StoBe Documentation*. Accessed July 2011.

19. C. Zhang, H. Chen, Y. Chen, Z. Wei, Z. Pu. *Acta Phys. -Chim. Sin*. **24**, 1353 (2008).

20. P. N. Day, K. A. Nguyen, R. Pachter. *J. Phys. Chem. B.* **109**, 1803 (2005).

21. A. D. McLean, G. S. Chandler. *J. Chem. Phys.*, **72,** 5639 (1980).

22. C. Lee, W. Yang, R. G. Parr. *Phys. Rev. B.* **37,** 785 (1988).

23. T. Regier, J. Krochak, T.K. Sham,Y.F. Hu, J. Thompson, R.I.R. Blyth. *Nucl. Instrum. Methods Phys. Res., Sect. A.* **582**, 93 (2007).

24. J. J., Jia, T. A. Callcott, J. Yurkas, A. W. Ellis, F. J. Himpsel, M. G. Samant, J. Stöhr, D. L. Ederer, J. A. Carlisle, E. A. Hudson, L. J. Terminello, D.K. Shuh, R.C.C. Perera. *Rev. Sci. Instrum*. **66**, 1394 (1995).

25. en.wikipedia.org/wiki/Synchrotron. Synchrotron. (2010).

26. H. Wiedemann. *Particle Accelerator Physics.* Springer-Verlag: Berlin Heidelberg: New York (2007).

27. http://imglib.lbl.gov/ImgLib/COLLECTIONS/BERKELEY-LAB. Radiation from an insertion device. (2011).

28. www.als.lbl.gov. High Resolution and Flux for Materials and Surface Science: Beam line 8.0.1 (2010).

29. M. O. Krause. *J. Phys. Chem. Ref. Data* **8**, 307 (1979).

30. C. R. McNeill, N. C. Greenham. *Adv. Mater*. **21**, 3840 (2009).

31. F.-X. Xie, W. C. H. Choy, X. Zhu, X. Li, Z. Li, C. Liang. *App. Phys. Lett*. **98**, 243302 (2011).

32. B. L. Henke, E. M. Gullikson, J. C. Davis. *At. Data Nucl. Data Tables*. **54,** 181 (1993).

33. A. Salleo, R. J. Kline, D. M. DeLongchamp, and M. L. Chabinyc. *Adv. Mater*. **22**, 3812 (2010).

34. M. G. Samant, J. Stöhr, H. R. Brown, T. P Russell, J. M. Sands, S. K. Kumar, *Macromolecules*. **29**, 8334 (1996).

35. J. Stöhr, D. Outka. *Phys. Rev. B*. **36,** 7891 (1987).

36. J. Stöhr. *NEXAFS Spectroscopy*. Springer-Verlag: Berlin (1996).

37. T. Beetz, C. Jacobsen. *J. Synchrotron Rad.* **10**, 280-283 (2003).

38. T. Coffey, S. G. Urquhart, H. Ade. *J. Electron Spectrosc. Relat. Phenom*. **122**, 65 (2002).

39. E. G. Rightor, A. P. Hitchcock, H. Ade, R. D. Leapman, S. G. Urquhart, A. P. Smith, G. Mitchell, D. Fischer, H. J. Shin, T. Warwick. *J. Phys. Chem. B.* **101**, 1950 (1997).

40. S. Y. Bae, K. H. Jung, M. H. Hoang, K. H. Kim, T. w. Lee, M. J. Choa, J.-I. Jin, D. H. Lee, D. S. Chung, C. E. Park, D. H. Choi. *Synth. Met*. **160**, 1022 (2010).

41. M. McDowell, I. G. Hill, J. E. McDermott, S. L. Bernasek, J. Schwartz. *App. Phys. Lett.* 88, 073505 (2006).

42. S. Ando, J.-I. Nishida, E. Fujiwara, H. Tada, Y. Inoue, S. Tokito, Y. Yamashita. *Chem. Mater*. **17**, 1261 (2005).

43. H. Meng, F. Sun, M. B. Goldfinger, F. Gao, D. J. Londono, W. J. Marshal, G. S. Blackman, K. D. Dobbs, D. E. Keys. *JACS*. **128**, 9304 (2006).

44. J.-H. Park, D. S. Chung, J.-W. Park, T. Ahn, H. Kong, Y. K. Jung, J. Lee, M. H. Yi, C. E. Park, S.-K. Kwon, H.-K. Shim. *Org. Lett*. **9**, 2573 (2007).

45. R. Schmidt, S. Göttling, D. Leusser, D. Stalke, A.-M. Krause, F. Würthner. *J. Mater. Chem.* **16**, 3708 (2006).

46. M. Mas-Torrent, C. Rovira. *Chem. Rev*. *In Press*.doi:10.1021/cr100142w. (2011).

47. J. E. Anthony. *Chem. Rev.* **106**, 5028 (2006).

48. J.-L. Brédas, D. Beljonne, V. Coropceanu, J. Cornil. *Chem. Rev.* **104**, 4971 (2004).

49. L. H. Jimison , A. Salleo , M. L. Chabinyc , D. P. Bernstein , M. F.Toney. *Phys. Rev. B.* **78**, 125319 (2008).

50. J. C. Hummelen, B. W. Knight, F. Lepeq, F. J. Wudl. *Org. Chem*. **60**, 532 (1995).

51. Y. A.M. Ismail, T. Soga, T. Jimbo. *Sol. Energy Mater. and Sol. Cells*. **93**, 1582 (2009).

52. P. H. Wobkenberg, D. D. C. Bradley, D. Kronholm, J. C. Hummelen, D. M. de Leeuw, M. Cölle, T. D. Anthopoulos, *Synth. Met.* **158**, 468 (2008).

53. B. Christoph, U. Scherf, V. Dyakonov. *Organic Photovoltaics: Materials, Device Physics, and Manufacturing Technologies*: Wiley-VCH Verlag GmbH&Co. KGaA: Weinheim (2008).

54. D. S. Germack, C. K. Chan, B. H. Hamadani, L. J. Richter, D. A. Fischer, D. J. Gundlach, D. M. Delongchamp, *Appl. Phys. Lett*. **94**, 233303 (2009).

55. D. M. DeLongchamp, S. Sambasivan, D. A. Fisher, E. K. Lin, P. Chang, A. R. Murphy, J. M. J. Frechet, V. Subramanian. *Adv. Mater*. **17**, 2340 (2005).

56. Y. Wang, M. Alcami, F. Martin. *ChemPhysChem*. **9**, 1030 (2008).

57. D. Ecija, R. Otero, L. Sanchez, J. M. Gallego, Y. Wang, M. Alcami, F. Martin, N. Martin, R. Miranda. *Angew*. *Chem. Int. Ed*. **46**, 7874 (2007).

58. J. M. Napoles-Duarte, M. Reyes-Reyes, J. L. Ricardo-Chavez, R. Garibay-Alonso, R. Lopez-Sandoval. *Phys. Rev. B.* **78**, 035425 (2008).

59. X. Yang, J. K. J. van Duren, M. T. Rispens, J. C. Hummelen, R. A. J. Janssen, M. A. J. Michels, J. Loos. *Adv. Mater*. **16**, 802 (2004).

60. Z. Zhang, P. Han, X. Liu, J. Zhao, H. Jia, F. Zeng, B. J. Xu. *J. Phys. Chem. C.* 112,19158 (2008).

61. K. Akaike, K. Kanai, H. Yoshida, J. Tsutsumi, T. Nishi, N. Sato, Y. Ouchi, K. J. Seki, *Appl. Phys. Lett.* **104**, 023710 (2008).

62. A. Patnaik, K. K. Okudaira, A. Kera, H. Setoyama, K. Mase, N. J. Ueno. *J. Chem. Phys.* **122**, 154703 (2005).

63. A. J. Maxwell, P. A. Bruhwiler, D. Arvantis, J. Hasselstrom, N. Matensson. *Chem. Phys. Lett*. **260**, 71 (1996),

64. D. Kondo, K. Sakamoto, H. Takeda, F. Matsui, K. Amemiya, T. Ohta, W. Uchida, A. Kasuya. *Surf. Sci*. **514**, 337 (2002).

65. H. Werner, T. Schedel-Niedrig, M. Wohlers, D. Herein, B. Herzog, R. Schlogl, M. Keil, A. M. Bradshaw, J. J. Kirschner. *Chem. Soc., Faraday Trans.* **90**, 403 (1994).

66. S.G. Urquhart, H. J. Ade. *Phys. Chem. B*. **106**, 8531 (2002).

67. J. Y. Kim, K. Lee, N. E. Coates, D. Moses, T. Nguyen, M. Dante, A. J. Heeger. *Science*. **317**, 222 (2007).

68. T. W. Lee, D. C. Kim, N. S. Kang, J. W. Yu, M. J. Cho, K. H. Kim, D. H. Choi. *Chem. Lett*. **37**, 866 (2008).

APPENDIX: StoBe Input Files

In this appendix, run files required to perform a complete XAS simulation following a geometry optimization are listed. The keywords which define the occupation of molecular orbitals are discussed following the atomic coordinates. The file shown is identical in structure to those input to StoBe, which runs on a computer cluster owned by the Beam Team Research Group headed by Dr. Alex Moewes at the University of Saskatchewan.

a) Slater Transition State XAS run file

This file places the core hole at site C1, and performs a calculation of the total XAS spectrum resulting from excitation of this single atom. Similar files are required for each atom being excited. The keyword lines shown below define the alfa and beta orbital occupations, with a half core hole placed in the alfa core level of C1. Note that all atoms not being excited have a modified nuclear charge of +4, and corresponding effective core potential basis sets are used at the end of the file. Also, the atomic coordinates used in this calculation are those that resulted from a previous geometry optimization.

```
alfa 108
beta 108
sym 1
alfa 108 1 3 0.5
beta 108 0
end
```

```
#!/bin/csh -f
ln -s /opt/StoBe/Basis/baslib.new7 fort.3
ln -s /opt/StoBe/Basis/symbasis.new fort.4
cat >help.inp <</.
title
BHT no ethynyl C1 XAS
nosy
cartesian angstrom
```

S1	-1.08801283	-5.03949978	-2.00067200	16.0000
S2	3.59107099	6.61373137	1.52312322	16.0000
C1	-1.67919269	-8.53345556	-1.75205337	6.0000
C2	3.57805697	3.44552495	1.14748832	4.0000
C3	3.65947037	2.13738314	0.74113340	4.0000
C4	2.31126085	4.11055470	1.27585076	4.0000
C5	1.16285531	3.39190894	0.97090291	4.0000
C6	2.48873448	1.37013345	0.43100065	4.0000
C7	1.19877345	2.02349220	0.56536265	4.0000
C8	-1.32259118	1.97365721	0.40265665	4.0000
C9	0.34570045	-4.19886024	-1.40348774	4.0000
C10	3.90444091	-0.64536117	-0.12075436	4.0000
C11	-3.21250057	3.12362063	-0.63186293	4.0000
C12	-1.93382814	2.15501335	1.65678249	4.0000
C13	3.51815156	10.03300908	0.97290778	4.0000
C14	1.43271188	-5.05550569	-1.45543514	4.0000
C15	4.62342251	-0.59538054	-1.32931229	4.0000
C16	-0.19841310	-6.52105385	-2.30096479	4.0000
C17	1.12627153	-6.35017990	-1.95667233	4.0000
C18	6.41273841	-1.92072284	-0.36118976	4.0000
C19	5.86735126	-1.22873482	-1.44933702	4.0000
C20	-3.80560643	3.30437902	0.62290263	4.0000
C21	-3.16438071	2.81415165	1.76710827	4.0000
C22	-0.88788041	-7.75457543	-2.82105022	4.0000
C23	2.23023720	5.50656576	1.72224170	4.0000
C24	1.16967672	6.17930456	2.30204581	4.0000
C25	2.70304787	7.95879513	2.22060116	4.0000
C26	1.43650380	7.54953910	2.57664684	4.0000
C27	3.30604811	9.33400998	2.32868711	4.0000
C28	0.01219295	1.29683935	0.28122312	4.0000
C29	2.56602003	0.02276874	0.01170470	4.0000
C30	1.38070680	-0.70445615	-0.27115669	4.0000
C31	0.08987365	-0.05523448	-0.12359970	4.0000
C32	-1.08042408	-0.84065059	-0.38709751	4.0000
C33	1.42225211	-2.06372998	-0.70456525	4.0000
C34	-0.99470220	-2.15217025	-0.78049257	4.0000
C35	0.27444397	-2.80169274	-0.96282613	4.0000
C36	-1.98292970	2.46283937	-0.73994290	4.0000
C37	5.70954343	-1.97385899	0.84822834	4.0000
C38	4.46598592	-1.34065987	0.96592021	4.0000
H1	6.41349977	-1.17710415	-2.39539212	1.0000
H2	4.19975701	-0.05493090	-2.18016465	1.0000
H3	6.12846608	-2.50962671	1.70433343	1.0000
H4	3.91708296	-1.38280921	1.91095017	1.0000
H5	2.62807434	9.93902260	2.95343279	1.0000
H6	4.26516549	9.28971898	2.87417276	1.0000

```
H7 0.19194034  3.88281628  1.02550839 1.0000
H8 4.49127859  3.99057781  1.39901649 1.0000
H9 4.63457490  1.65505707  0.65780359 1.0000
H10 -2.05963520 -0.37564493 -0.26143054 1.0000
H11  2.40233397 -2.51976291 -0.84264945 1.0000
H12 -1.91290193 -2.71962820 -0.95425238 1.0000
H13 -3.62279442  2.94230210  2.75175763 1.0000
H14 -3.70716809  3.49951199 -1.53194090 1.0000
H15 -1.52048841  2.32932705 -1.72173332 1.0000
H16 -1.56520807 -7.48471944 -3.64916851 1.0000
H17 -0.11520692 -8.40699954 -3.25933469 1.0000
H18 -2.45563139 -7.90233359 -1.29370508 1.0000
H19 -1.01719820 -8.88685341 -0.94713756 1.0000
H20 -1.43535529  1.77491302  2.55270116 1.0000
H21  0.22461898  5.69281903  2.54705882 1.0000
H22  0.71084877  8.22452922  3.03667339 1.0000
H23  2.43156438 -4.76603000 -1.12420659 1.0000
H24  1.86687821 -7.14575764 -2.06163658 1.0000
H25  7.38304503 -2.41607731 -0.45445956 1.0000
H26 -4.76471740  3.82340833  0.70771603 1.0000
H27  2.56913193 10.11862264  0.42302480 1.0000
H28  4.22191207  9.47248080  0.33840688 1.0000
H29  3.92671302 11.04570553  1.11560578 1.0000
H30 -2.17681196 -9.40959330 -2.19789618 1.0000
end
runtype startup
scftype direct
potential nonlocal be88 pd86
grid fine
multiplicity 1
virt all
charge 0
maxcycles 1000
econvergence 0.000001
dconvergence 0.000001
dmixing mdens 0.1
diis new 7
orbi 5d
fsym scfocc excited
alfa 108
beta 108
sym 1
alfa 108 1 3 0.5
beta 108 0
end
mulliken on
```

```
xray xas
remthreshold  1.D-6
end
ctrl
end
A-SULFUR (5,4;5,4)
A-SULFUR (5,4;5,4)
A-CARBON (5,2;5,2)
A-CARBON(+4) (3,3;3,3)
A-CARBON(+4) (3,3;3,3)
A-CARBON(+4) (3,3;3,3)
A-CARBON(+4) (3,3;3,3)
A-CARBON(+4) (3,3;3,3)
A-CARBON(+4) (3,3;3,3)
A-CARBON(+4) (3,3;3,3)
A-CARBON(+4) (3,3;3,3)
A-CARBON(+4) (3,3;3,3)
A-CARBON(+4) (3,3;3,3)
A-CARBON(+4) (3,3;3,3)
A-CARBON(+4) (3,3;3,3)
A-CARBON(+4) (3,3;3,3)
A-CARBON(+4) (3,3;3,3)
A-CARBON(+4) (3,3;3,3)
A-CARBON(+4) (3,3;3,3)
A-CARBON(+4) (3,3;3,3)
A-CARBON(+4) (3,3;3,3)
A-CARBON(+4) (3,3;3,3)
A-CARBON(+4) (3,3;3,3)
A-CARBON(+4) (3,3;3,3)
A-CARBON(+4) (3,3;3,3)
A-CARBON(+4) (3,3;3,3)
A-CARBON(+4) (3,3;3,3)
A-CARBON(+4) (3,3;3,3)
A-CARBON(+4) (3,3;3,3)
A-CARBON(+4) (3,3;3,3)
A-CARBON(+4) (3,3;3,3)
A-CARBON(+4) (3,3;3,3)
A-CARBON(+4) (3,3;3,3)
A-CARBON(+4) (3,3;3,3)
A-CARBON(+4) (3,3;3,3)
A-CARBON(+4) (3,3;3,3)
A-CARBON(+4) (3,3;3,3)
A-CARBON(+4) (3,3;3,3)
A-CARBON(+4) (3,3;3,3)
A-CARBON(+4) (3,3;3,3)
A-HYDROGEN (3,1;3,1)
```

```
A-HYDROGEN (3,1;3,1)
A-HYDROGEN (3,1;3,1)
A-HYDROGEN (3,1;3,1)
A-HYDROGEN (3,1;3,1)
A-HYDROGEN (3,1;3,1)
A-HYDROGEN (3,1;3,1)
A-HYDROGEN (3,1;3,1)
A-HYDROGEN (3,1;3,1)
A-HYDROGEN (3,1;3,1)
A-HYDROGEN (3,1;3,1)
A-HYDROGEN (3,1;3,1)
A-HYDROGEN (3,1;3,1)
A-HYDROGEN (3,1;3,1)
A-HYDROGEN (3,1;3,1)
A-HYDROGEN (3,1;3,1)
A-HYDROGEN (3,1;3,1)
A-HYDROGEN (3,1;3,1)
A-HYDROGEN (3,1;3,1)
A-HYDROGEN (3,1;3,1)
A-HYDROGEN (3,1;3,1)
A-HYDROGEN (3,1;3,1)
A-HYDROGEN (3,1;3,1)
A-HYDROGEN (3,1;3,1)
A-HYDROGEN (3,1;3,1)
A-HYDROGEN (3,1;3,1)
A-HYDROGEN (3,1;3,1)
A-HYDROGEN (3,1;3,1)
A-HYDROGEN (3,1;3,1)
A-HYDROGEN (3,1;3,1)
O-SULFUR (73111/6111/1)
O-SULFUR (73111/6111/1)
O-CARBON iii_iglo
O-CARBON(+4) (311/211)
O-CARBON(+4) (311/211)
O-CARBON(+4) (311/211)
O-CARBON(+4) (311/211)
O-CARBON(+4) (311/211)
O-CARBON(+4) (311/211)
O-CARBON(+4) (311/211)
O-CARBON(+4) (311/211)
O-CARBON(+4) (311/211)
O-CARBON(+4) (311/211)
O-CARBON(+4) (311/211)
O-CARBON(+4) (311/211)
O-CARBON(+4) (311/211)
O-CARBON(+4) (311/211)
```

O-CARBON(+4) (311/211)
O-CARBON(+4) (311/211)
O-CARBON(+4) (311/211)
O-CARBON(+4) (311/211)
O-CARBON(+4) (311/211)
O-CARBON(+4) (311/211)
O-CARBON(+4) (311/211)
O-CARBON(+4) (311/211)
O-CARBON(+4) (311/211)
O-CARBON(+4) (311/211)
O-CARBON(+4) (311/211)
O-CARBON(+4) (311/211)
O-CARBON(+4) (311/211)
O-CARBON(+4) (311/211)
O-CARBON(+4) (311/211)
O-CARBON(+4) (311/211)
O-CARBON(+4) (311/211)
O-CARBON(+4) (311/211)
O-CARBON(+4) (311/211)
O-CARBON(+4) (311/211)
O-CARBON(+4) (311/211)
O-CARBON(+4) (311/211)
O-CARBON(+4) (311/211)
O-HYDROGEN (41/1*)
O-HYDROGEN (41/1*)
O-HYDROGEN (41/1*)
O-HYDROGEN (41/1*)
O-HYDROGEN (41/1*)
O-HYDROGEN (41/1*)
O-HYDROGEN (41/1*)
O-HYDROGEN (41/1*)
O-HYDROGEN (41/1*)
O-HYDROGEN (41/1*)
O-HYDROGEN (41/1*)
O-HYDROGEN (41/1*)
O-HYDROGEN (41/1*)
O-HYDROGEN (41/1*)
O-HYDROGEN (41/1*)
O-HYDROGEN (41/1*)
O-HYDROGEN (41/1*)
O-HYDROGEN (41/1*)
O-HYDROGEN (41/1*)
O-HYDROGEN (41/1*)
O-HYDROGEN (41/1*)
O-HYDROGEN (41/1*)
O-HYDROGEN (41/1*)

```
O-HYDROGEN (41/1*)
O-HYDROGEN (41/1*)
O-HYDROGEN (41/1*)
O-HYDROGEN (41/1*)
O-HYDROGEN (41/1*)
O-HYDROGEN (41/1*)
O-HYDROGEN (41/1*)
P-CARBON(+4) (5:6)
P-CARBON(+4) (5:6)
P-CARBON(+4) (5:6)
P-CARBON(+4) (5:6)
P-CARBON(+4) (5:6)
P-CARBON(+4) (5:6)
P-CARBON(+4) (5:6)
P-CARBON(+4) (5:6)
P-CARBON(+4) (5:6)
P-CARBON(+4) (5:6)
P-CARBON(+4) (5:6)
P-CARBON(+4) (5:6)
P-CARBON(+4) (5:6)
P-CARBON(+4) (5:6)
P-CARBON(+4) (5:6)
P-CARBON(+4) (5:6)
P-CARBON(+4) (5:6)
P-CARBON(+4) (5:6)
P-CARBON(+4) (5:6)
P-CARBON(+4) (5:6)
P-CARBON(+4) (5:6)
P-CARBON(+4) (5:6)
P-CARBON(+4) (5:6)
P-CARBON(+4) (5:6)
P-CARBON(+4) (5:6)
P-CARBON(+4) (5:6)
P-CARBON(+4) (5:6)
P-CARBON(+4) (5:6)
P-CARBON(+4) (5:6)
P-CARBON(+4) (5:6)
P-CARBON(+4) (5:6)
P-CARBON(+4) (5:6)
P-CARBON(+4) (5:6)
P-CARBON(+4) (5:6)
P-CARBON(+4) (5:6)
P-CARBON(+4) (5:6)
P-CARBON(+4) (5:6)
X-DUMMY
X-DUMMY
```

```
X-FIRST
end
/.
/opt/StoBe/bin/StoBe.x <help.inp >& BHTC1xas.out
mv fort.11 BHTC1xas.xas
```

In order to compute the ground state and full core hole calculations, only those keywords shown in italics need to be modified to redefine the core hole. In the case of the ground state, the entire set of excitation keywords are removed, and the system is allowed to populate by the aufbau principle. Note that the XAS spectrum itself is generated by the Slater transition file, with only the total energy is recorded from the other two calculations for calibration.

b) Ground State

These keywords are removed entirely:

```
fsym scfocc excited
alfa 108
beta 108
sym 1
alfa 108 1 3 0.5
beta 108 0
end
mulliken on
xray xas
remthreshold  1.D-6
end
```

Then they are simply replaced with:

```
fsym aufbau
```

c) Full core hole

A full core hole is added by increasing the total alpha occupation by one electron, and placing a core hole at the site of excitation.

```
alfa 109
beta 108
sym 1
alfa 109 1 3 0.0
beta 108 0
end
```

d) Broadening

In addition to calculating the XAS, broadening is often desired for the purpose of presentation. Initially the output file simply contains oscillator strengths which may be broadened using Gaussian type broadening in an attempt to mimic the lineshape of the measurement. Shown below is a typical broadening file for C1, which uses a broadening with a Gaussian of 0.6 eV FWHM up to 288 eV, with an additional broadening that increases linearly up to 7 eV FWHM at 300 eV.

```
#!/bin/csh -f
ln -s BHTC1xas.xas fort.1
cat >help.inp <</.
title
BHT C1 1s Xray absorption spectrum
print
range 280 309.9
points 300
width 0.6 7 288 300
xray xas
total 1
end
/.
/opt/StoBe/bin/xrayspec.x < help.inp > /home/paul/BHT/Out/BHTC1ver.out
mv XrayT001.out /home/paul/BHT/Out/BHTC1xasB.out
rm help.inp fort.*
```